arXiv:2301.02775v1 [astro-ph.SR] 7 Jan 2023

The messy death of a multiple star system and the resulting planetary nebula as observed by JWST

Orsola De Marco[1,2*], Muhammad Akashi[3,4], Stavros Akras[5], Javier Alcolea[6], Isabel Aleman[7], Philippe Amram[8], Bruce Balick[9], Elvire De Beck[10], Eric G. Blackman[11,12], Henri M. J. Boffin[13], Panos Boumis[5], Jesse Bublitz[14], Beatrice Bucciarelli[15], Valentin Bujarrabal[6], Jan Cami[16,17,18], Nicholas Chornay[19], You-Hua Chu[20], Romano L.M. Corradi[21,22], Adam Frank[23], Guillermo García-Segura[24], D. A. García-Hernández[22,25], Jorge García-Rojas[22,25], Veronica Gómez-Llanos[22,25], Denise R. Gonçalves[26], Martín A. Guerrero[27], David Jones[22,25], Amanda I. Karakas[28,29], Joel H. Kastner[30,31], Sun Kwok[32], Foteini Lykou[33,34], Arturo Manchado[22,25,35], Mikako Matsuura[36], Iain McDonald[37,38], Ana Monreal-Ibero[39], Hektor Monteiro[7], Paula Moraga Baez[31], Christophe Morisset[24], Brent Miszalski[40], Shazrene S. Mohamed[41,42,43,44], Rodolfo Montez Jr.[45], Jason Nordhaus[46,47], Claudia Mendes de Oliveira[48], Zara Osborn[28,29], Masaaki Otsuka[49], Quentin A. Parker[50,51], Els Peeters[16,17,18], Bruno C. Quint[52], Guillermo Quintana-Lacaci[53], Matt Redman[54], Ashley J. Ruiter[55], Laurence Sabin[24], Carmen Sánchez Contreras[56], Miguel Santander-García[6], Ivo Seitenzahl[55], Raghvendra Sahai[57], Noam Soker[3], Angela K. Speck[58], Letizia Stanghellini[59], Wolfgang Steffen[60], Jesús A. Toalá[61], Toshiya Ueta[62], Griet Van de Steene[63], Eva Villaver[56], Paolo Ventura[64], Wouter Vlemmings[65], Jeremy R. Walsh[13], Roger Wesson[36], Hans van Winckel[66] and Albert A. Zijlstra[38]

[1*]School of Mathematical and Physical Sciences, Macquarie University, Sydney, NSW 2109, Australia.
[2*]Astronomy, Astrophysics and Astrophotonics Research Centre, Macquarie University, Sydney, NSW 2109, Australia.
[3]Department of Physics, Technion, Haifa, 3200003, Israel.
[4]Kinneret College on the Sea of Galilee, Samakh 15132, Israel.
[5]Institute for Astronomy, Astrophysics, Space Applications and Remote Sensing, National Observatory of Athens, GR 15236 Penteli, Greece.
[6]Observatorio Astronómico Nacional (OAN/IGN), Alfonso XII, 3, 28014 Madrid, Spain.
[7]Instituto de Física e Química, Universidade Federal de Itajubá, Av. BPS 1303, Pinheirinho, Itajubá 37500-903, Brazil.
[8]Aix-Marseille Univ., CNRS, CNES, LAM (Laboratoire d'Astrophysique de Marseille), Marseille, France.
[9]Astronomy Department, University of Washington, Seattle, WA 98105-1580, USA.
[10]Department of Space, Earth and Environment, Chalmers University of Technology, S-41296 Gothenburg, Sweden.
[11]Department of Physics and Astronomy, University of Rochester, Rochester, NY 14627, USA.
[12]Laboratory for Laser Energetics, University of Rochester, Rochester NY, 14623, USA.
[13]European Southern Observatory, Karl-Schwarzschild Strasse 2, D-85748 Garching, Germany.
[14]Green Bank Observatory, 155 Observatory Road, PO Box 2, Green Bank, WV 24944, USA.
[15]INAF - Osservatorio Astrofisico di Torino, Via Osservatorio 20, 10023, Pino Torinese, Italy.
[16]Department of Physics & Astronomy, University of Western Ontario, London, ON, N6A 3K7, Canada.
[17]Institute for Earth and Space Exploration, University of Western Ontario, London, ON, N6A 3K7, Canada.
[18]SETI Institute, 399 Bernardo Avenue, Suite 200, Mountain View, CA 94043, USA.
[19]Institute of Astronomy, University of Cambridge, Madingley Road, Cambridge CB3 0HA, UK.
[20]Institute of Astronomy and Astrophysics, Academia Sinica (ASIAA), No. 1, Section 4, Roosevelt Road, Taipei 10617, Taiwan.

[21]GRANTECAN, Cuesta de San José s/n, E-38712, Breña Baja, La Palma, Spain.
[22]Instituto de Astrofísica de Canarias, E-38205 La Laguna, Tenerife, Spain.
[23]Department of Physics and Astronomy, University of Rochester, Rochester, NY 14627, USA.
[24]Instituto de Astronomía, Universidad Nacional Autónoma de México, Km. 107 Carr. Tijuana-Ensenada, 22860, Ensenada, B. C., Mexico.
[25]Departamento de Astrofísica, Universidad de La Laguna, E-38206 La Laguna, Tenerife, Spain.
[26]Observatório do Valongo, Universidade Federal do Rio de Janeiro, Ladeira Pedro Antonio 43, Rio de Janeiro 20080-090, Brazil.
[27]Instituto de Astrofísica de Andalucía, IAA-CSIC, Glorieta de la Astronomía, s/n, E-18008, Granada, Spain.
[28]School of Physics & Astronomy, Monash University, Clayton VIC 3800, Australia.
[29]ARC Centre of Excellence for All Sky Astrophysics in 3 Dimensions (ASTRO 3D).
[30]Center for Imaging Science, Rochester Institute of Technology, Rochester, NY 14623, USA.
[31]School of Physics and Astronomy and Laboratory for Multiwavelength Astrophysics, Rochester Institute of Technology, USA.
[32]Department of Earth, Ocean, and Atmospheric Sciences, University of British Columbia, Vancouver, Canada.
[33]Konkoly Observatory, Research Centre for Astronomy and Earth Sciences, Eötvös Loránd Research Network (ELKH), Konkoly-Thege Miklós út 15-17, 1121 Budapest, Hungary.
[34]CSFK, MTA Centre of Excellence, Konkoly-Thege Miklós út 15-17, 1121 Budapest, Hungary.
[35]Consejo Superior de Investigaciones Científicas, Spain.
[36]School of Physics and Astronomy, Cardiff University, The Parade, Cardiff CF24 3AA, UK.
[37]Department of Physical Sciences, The Open University, Walton Hall, Milton Keynes, MK7 6AA, UK.
[38]Jodrell Bank Centre for Astrophysics, Department of Physics and Astronomy, The University of Manchester, Oxford Road M13 9PL Manchester, UK.

[39]Leiden Observatory, Leiden University, Niels Bohrweg 2, NL 2333 CA Leiden, The Netherlands.
[40]Australian Astronomical Optics, Faculty of Science and Engineering, Macquarie University, North Ryde, NSW 2113, Australia.
[41]Department of Physics, University of Miami, Coral Gables, FL 33124, USA.
[42]South African Astronomical Observatory, P.O. Box 9, 7935 Observatory, South Africa.
[43]Astronomy Department, University of Cape Town, 7701 Rondebosch, South Africa.
[44]NITheCS National Institute for Theoretical and Computational Sciences, South Africa.
[45]Center for Astrophysics, Harvard & Smithsonian, 60 Garden Street, Cambridge, MA 02138, USA.
[46]Center for Computational Relativity and Gravitation, Rochester Institute of Technology, Rochester, NY 14623, USA.
[47]National Technical Institute for the Deaf, Rochester Institute of Technology, Rochester, NY 14623, USA.
[48]Departamento de Astronomia, Instituto de Astronomia, Geofísica e Ciências Atmosféricas da USP, Cidade Universitária, 05508-900, São Paulo, SP, Brazil.
[49]Okayama Observatory, Kyoto University, Honjo, Kamogata, Asakuchi, Okayama, 719-0232, Japan.
[50]Department of Physics, CYM Physics Building, The University of Hong Kong, Pokfulam, Hong Kong SAR, PRC.
[51]Laboratory for Space Research, Cyberport 4, Cyberport, Hong Kong SAR, PRC.
[52]Rubin Observatory Project Office, 950 N. Cherry Ave., Tucson, AZ 85719, USA.
[53]Dept. of Molecular Astrophysics. IFF-CSIC. C/ Serrano 123, E-28006, Madrid, Spain.
[54]Centre for Astronomy, School of Physics, National University of Ireland Galway, Galway H91 CF50, Ireland.
[55]University of New South Wales, Australian Defence Force Academy, Canberra, Australian Capital Territory, Australia.
[56]Centro de Astrobiología (CAB), CSIC-INTA, Camino Bajo del Castillo s/n, ESAC campus, 28692, Villanueva de la Cañada, Madrid, Spain.

[57]Jet Propulsion Laboratory, California Institute of Technology, CA 91109, Pasadena, USA.
[58]University of Texas at San Antonio, Department of Physics and Astronomy, Applied Engineering and Technology Building, One UTSA Circle, San Antonio, TX 78249, United States.
[59]NSF's NOIRLab, 950 N. Cherry Ave., Tucson, AZ 85719, USA.
[60]ilumbra, AstroPhysical MediaStudio, Hautzenbergstrasse 1, 67661 Kaiserslautern, Germany.
[61]Instituto de Radioastronomía y Astrofísica, UNAM, Antigua Carretera a Pátzcuaro 8701, Ex-Hda. San José de la Huerta, Morelia 58089, Mich., Mexico.
[62]Department of Physics and Astronomy, University of Denver, 2112 E Wesley Ave., Denver, CO 80208, USA.
[63]Royal Observatory of Belgium, Astronomy and Astrophysics, Ringlaan 3, 1180 Brussels, Belgium.
[64]INAF – Osservatorio Astronomico di Roma, Via Frascati 33, I-00040, Monte Porzio Catone (RM), Italy.
[65]Onsala Space Observatory, Department of Space, Earth and Environment, Chalmers University of Technology, Onsala, Sweden.
[66]Institute of Astronomy, KULeuven, Celestijnenlaan 200D, B-3001 Leuven, Belgium.

*Corresponding author(s). E-mail(s): orsola.demarco@mq.edu.au;

Abstract

Planetary nebulae (PNe), the ejected envelopes of red giant stars, provide us with a history of the last, mass-losing phases of 90% of stars initially more massive than the Sun. Here, we analyse James Webb Space Telescope (JWST) Early Release Observation (ERO) images of the PN NGC 3132. A structured, extended H_2 halo surrounding an ionised central bubble is imprinted with spiral structures, likely shaped by a low-mass companion orbiting the central star at ∼40–60 AU. The images also reveal a mid-IR excess at the central star interpreted as a dusty disk, indicative of an interaction with another, closer companion. Including the previously known, A-type visual companion, the progenitor of the NGC 3132 PN must have been at least a stellar quartet. The JWST images allow us to generate a model of the illumination, ionisation and hydrodynamics of the molecular halo, demonstrating the power of JWST to investigate complex stellar outflows. Further, new measurements of the A-type visual companion allow us to derive the value for

the mass of the progenitor of a central star to date with excellent precision: $\mathbf{2.86 \pm 0.06\,M_{\odot}}$. These results serve as pathfinders for future JWST observations of PNe providing unique insight into fundamental astrophysical processes including colliding winds, and binary star interactions, with implications for supernovae and gravitational wave systems.

Keywords: stars: AGB and post-AGB, stars: evolution, ISM: jets and outflows, ISM: molecules, planetary nebulae: individual: NGC 3132

Main

Introduction

Planetary nebulae (PNe) are the ejected envelopes of intermediate-mass (∼1–8 $M_{\odot}$) stars that have recently terminated their asymptotic giant branch (AGB) stage of evolution. Moving outwards from the hot pre-white dwarf star ($T \sim 10^5$ K) that is the progeny of the AGB star, the structure of a canonical quasi-spherical PN consists of a hot, sparse, wind-heated bubble ($T \sim 10^7$K) surrounded by a dense shell of displaced, ionised AGB gas ($T \sim 10^4$ K), which in turn may still be surrounded by "pristine," cold ($T \sim 10^2$ K), molecule- and dust-rich AGB ejecta. On the other hand, if the progenitor star interacted with a companion(s) during its post-main sequence evolution, we would expect departures from spherical symmetry, perhaps including spiral structures and arcs [e.g., 1–3], the presence of a dense, molecule-rich torus [e.g., 4], one or more pairs of polar lobes formed by fast, collimated outflows and jets [e.g., 5, 6], and/or a dusty, circumbinary disk [7]. The type of interaction depends on the orbital radius, and ranges from common envelope evolution for close binaries [8], to accretion disks and gravitational focussing of the wind for wider systems [9–11], to displacement of the central star from the geometric centre of the nebula for the widest systems [12].

The first Hubble Space Telescope (HST) images of PNe revealed a breath-taking new world of details and far more complex structures than had been gleaned from ground-based images [e.g., 13, 14]. The superb spatial resolution of HST, combined with high-resolution, kinematic mapping, enabled the construction of detailed 3D, morpho-kinematic models, which, together with hydrodynamic models [e.g., 15, 16], started to connect our understanding of the evolution of the structures and kinematics of PNe with their possible binary star origins [e.g., 17–19].

The James Webb Space Telescope (JWST), with its superb sensitivity and high spatial resolution from near- to mid-IR, is now poised to enable a leap of similar magnitude in our understanding of PNe. This journey began when JWST released near-IR and mid-IR images of just one PN, NGC 3132, as part of its ERO program. NGC 3132 is a nearby ($D \sim 750$ pc), molecule-rich [20, 21], ring-like PN, long known to harbour a visual binary comprising the central (progenitor) star and an A star companion. In this paper we show that

the JWST ERO images contain multiple, new lines of evidence that NGC 3132 is the recent product of a hierarchical multiple progenitor stellar system, which has experienced both indirect and direct interactions involving one or more components. Such binary interactions have taken on new importance in the era of gravitational wave detectors (LIGO [22], LISA [23]) and ambitious transient surveys [24]. Indeed, PNe like NGC 3132 offer unique insight into the formation pathways of the close, single and double degenerate binaries that are eventual gravitational wave sources and (perhaps) type Ia supernova progenitors [25–27].

Results

A flocculent molecular halo surrounding an ionised bubble

Figure 1 displays colour overlays of NIRCam and MIRI images of NGC 3132 that highlight JWST's clean separation of the PN's ionised (H II) and molecular (H_2) regions. The full resulting JWST image suite, along with basic information, is presented in Specification of JWST NIRCam and MIRI imaging and Supplementary Figure 1. The images reveal, for the first time, the extent and detailed structure of the halo of molecular gas that lies exterior to the nebula's central, ionised cavity and its bright and thin, peripheral elliptical ring (cf. [28]). This molecular halo is well detected in rovibrational H_2 emission at 2.12 μm (1–0 S(1)), 4.7 μm (0–0 S(9)), and 7.7 μm (0–0 S(5)) out to 60 arcsec ($\sim$0.22 pc at the adopted distance of 754 pc, see Properties and distance of NGC 3132) from the central star. Spatially organised structures — arcs and patterns of spikes emanating radially outward — are observed in the halo H_2 emission on medium to large scales, while molecular arcs, loops, and knots are detected on size scales from $\sim$500 AU down to the limiting ($\sim$75 AU) resolution of the images. The typical thickness of the bright H_2 rings that surround the nebular core is $\sim 1-2$ arcsec ($\sim$750-1500 AU), measured at 2.1, 4.7 and 7.7 μm.

Figure 1 conclusively demonstrates that the molecular gas is much clumpier than the ionised gas component of NGC 3132 (see also Supplementary Figure 3). In hydrogen recombination lines and [S III] emission (Figure 1, top-left), the nebula's central ionised cavity (within $\sim$25 arcsec of the central star) appears as a relatively smooth elliptical region that is bounded by a single, sharped-edged ring; whereas in H_2 (Figure 1, bottom-left), this same central region appears as a far more complex system of clumpy filaments. The regions in and around this bright, inner H_2 ring system contain as many as 20 dense clumps (knots) per square arcsec, implying the total number of H_2 knots in this region exceeds 10^4. The H_2 knots in the outer (halo) region are less distinct and further apart.

The presence of radially-directed spike features in the H_2 halo indicates that direct irradiation by UV photons, leaking through less dense gas between the inner ring system's H_2 knots, are most likely responsible for the excitation of the IR H_2 lines in the extended halo, although shock excitation cannot be

completely ruled out (see [29] and references therein). The relative lack of H_2 halo emission to the East-Northeast and West-Southwest of the central star then indicates a general lack of central star UV illumination, as opposed to lack of halo molecular mass in those directions (see Discussion). Measurements of the extinction of background nebulosity through representative knots suggests typical knot densities of $\sim 10^6$ cm^{-3} and masses of $\sim 10^{-5}$ M$_\odot$ (see Densities, masses and excitation of the H_2 knots), suggesting a total H_2 mass of ∼0.1 M$_\odot$ in the central ring region.

The system of (broken) concentric arcs revealed in the H_2 halo by the JWST images is similar to those observed in the extended, dusty envelopes of many AGB stars, proto-PNe and PNe (e.g., [3, 30, 31]). A widely accepted scenario to explain the formation of such arc systems is the modulation of an AGB wind by a stellar or substellar companion, creating 3D spiral-like patterns along the orbital plane [see 1, 32–35, and references therein]. The average angular distance between the arc structures, 2 arcsec, implies an orbital period of 290-480 years and an orbital separation of 40-60 AU between the central star and the companion that shapes the mass loss. Here, we have assumed a companion mass of 0.2 M$_\odot$, the highest mass main-sequence star that could hide in the present-day central star's glare yet still form a visible arc system (other parameters are an expansion velocity in the range 15-25 km s^{-1} [31] and an assumed late-AGB central star mass of ∼0.8 M$_\odot$; likely still 0.1-0.2 M$_\odot$ larger than the post-AGB mass). The bright A2 V visual companion seen at ∼1300 AU projected separation from the central star cannot be responsible, suggesting (at least) a triple system in a stable configuration.

The dusty central star

In the MIRI images obtained at wavelengths longer than 10 μm, the faint central star appears as bright or brighter than its A2 V main sequence visual companion [36]; see Figure 2. This infrared excess was undetectable in the mid-infrared at lower spatial resolution (e.g., in WISE images [37]) because of the surrounding bright nebulosity. The JWST-discovered IR excess indicates that a considerable amount of warm dust is present around the ultra-hot (∼110 kK) PN central star. The thermal infrared source appears marginally extended in the 11.3 and 12.8 μm MIRI images with an apparent size of ∼300 AU (FWHM) at 12.8 μm (see PSF measurements of the central star).

The bottom panel of Figure 2 displays the central star's near-IR to mid-IR spectral energy distribution fitted by a combination of a hot stellar photosphere represented by a blackbody curve and two curves to fit the infrared data points. The two curves are generated with a model that follows closely that of [38] for the Helix nebula. A number of 100 μm grains are taken as blackbody spheres with temperatures set by absorption and re-emittance of the stellar luminosity (200 L$_\odot$; a correction factor is then applied to simulate a grain size distribution between 60 and 1000 μm, as done by [38]). The temperature varies as $d^{0.5}$, where d is the distance to the star. The surface density of the disk is taken as constant. The resulting blackbody radiation is calculated at each radius, and

the emission is summed over all radii. A better model will require radiative transfer, actual dust emissivities, a range of grains sizes, and for the silicate feature, the inclination of the disk. This will be explored in a future paper.

The best-fit model disk has an inner radius of 55 AU and outer radius 140 AU, and a dust mass of 3×10^{26} g or 2×10^{-7} $M_\odot$ (approximately 0.05 Earth masses). The dust temperature range (inner to outer radius) is 130 to 80 K. The outer radius of 140 AU, though poorly constrained, is consistent with the deconvolved half-width of the marginally extended mid-IR source. These dimensions resemble those inferred for the disk orbiting the central star of the Helix (35–150 AU; [38]), but the dust mass is somewhat smaller (cfr. 0.13 earth masses). The outer radius could be slightly larger, if the 18 μm flux is underestimated because of detector saturation. An additional inner, hotter disk — with radius between 3 and 8 AU, a temperature between 550 to 335 K (inside to outside) and a very small mass of 2×10^{22} g (approximately 0.02 times the mass of Ceres) — is needed to fit the 3.5 and 7 μm fluxes. While this model does not constrain the geometry of the distribution to be that of a disk, the reasoning behind a disk structure is based on a physical reasoning whereby only a rotating Keplerian disk can be shown to be stable and relatively long-lived, while other structures, such as shells, are easily shown to be unstable [39].

The A2 V companion is slightly evolved [36] and has a mass of $M_{\rm A2V} = 2.40 \pm 0.15\,M_\odot$, using the PARSEC isochrones. Its visual companion, the PN central star, must have descended from a more massive star, as it has evolved faster. Extrapolating the same PARSEC isochrone gives an initial main sequence mass for the central star of $M_{\rm i} = 2.86 \pm 0.06\,M_\odot$. This is potentially the most precise initial mass for any PN central star or white dwarf yet determined. We estimate the error to be 0.16 $M_\odot$ if we add systematic effects between different isochrone models (see Central star system's masses).

The current (near-final) mass of a PN central star descended from such a $\sim$2.9 $M_\odot$ progenitor is predicted to be $M_f \sim 0.66 \pm 0.05\,M_\odot$ based on initial-final mass relations [40], albeit with larger systematic uncertainties that are dependent on details of the mass loss process adopted by the models. It is noteworthy that photoionisation models of the nebula require a cooler, dimmer and overall less massive central star (0.58 ± 0.03 $M_\odot$) than what we have found.

We find that we can reconcile the mass of the star today and that of the photoionisation model, while also matching the nebular abundances and the nebular age, if we assume that the AGB evolution of a 2.86 $M_\odot$ star, was interrupted by a binary interaction that ejected the envelope. We conjecture that the AGB evolution was interrupted at a core mass of 0.61 $M_\odot$, because for larger values, the C/O ratio of the stellar envelope gas would increase above unity (counter to the observation of crystalline silicate grains). At larger masses the N/O ratio would also increase above the observed value of 0.42.

Discussion

The first striking discovery of JWST is the presence of the dusty disk around the ultra-hot central star. This indicates that JWST can accurately detect dusty disks lighter than Ceres, as far as ∼700 pc away. For our PN, the presence of such a disk orbiting the PN central star favours a close binary interaction, where the companion either merged with the primary star, or is still in orbit but is undetected (mass < 0.2 $M_\odot$; based on an unresolved or barely resolved, equal-brightness companion); in either case, the companion has donated a substantial fraction of its angular momentum to the gas [41, 42]. Observationally, such disks around PN central stars, though rare, appear to be by and large associated with known or strongly suspected binarity [39] and may be related to circumbinary disks detected around other classes of post-AGB binary stars [43].

An interacting binary scenario is reinforced by the shape of the ionised cavity, which represents the inner, most recent mass-loss phase, when the already hot central star emitted a fast, tenuous wind. Pairing the JWST images with spatially resolved spectroscopy we constructed a 3D visualisation of this cavity (see Morpho-kinematic modelling in Supplementary Material). In Figure 3 we show that this inner cavity is inferred to be an expanding prolate ellipsoid with its long axis tilted at approximately 30 deg to the line of sight. Its surface is not smooth and presents instead a number of protuberances, most of which can be paired via axes passing through, or very near the central star. Prolate cavities such as these, with misaligned structures, are common in PN and are likely sculpted by jets from interacting binaries in the earlier, pre-PN phase of the nebula [44], with additional details added during the interaction between the AGB wind and post-AGB fast wind and via the process of PN ionisation.

The numerous protuberances clearly evident in the 3D reconstruction could arise from ionised gas breaking out of the inner cavity through an uneven outer shell. The apparent pairing between these protuberances may argue instead for the presence of intermittent and toppling jets [45]. To generate jets over such a wide range of axes, an interacting binary is not enough, and one would have to conjecture that the central star is or was a member of not just a close binary, but of an interacting *triple* system [46]. Recent studies of interactions in triple systems [47, 48] also argue for the possibility of interactions yielding complex ejecta.

Outside the ionised ellipsoid, one encounters material ejected earlier in the star's history. The AGB mass loss, at rates of up to $\sim 10^{-5}$ $M_\odot yr^{-1}$ and speeds of ∼10 km s^{-1} over a $\sim 10^5$ yr timescale [49], generates an enormous, expanding envelope of molecular gas and dust. The H_2 halo imaged by JWST constitutes the most recently ejected (inner) region of this AGB envelope. The spikes observed in the halo (Figure 1, right panel) show that the inner cavity is very porous, though less so near the minor axis where the cavity edges are brightest, densest, and least fractured.

The JWST images motivated 2D hydrodynamic simulations to replicate these flocculent structures. In Figure 4 we see two time snapshots towards the

end of a simulation where an inner, faster wind from the heating central star and its ionising radiation, plough into the dense AGB (halo) material (see Methods, Section 66). The fragmentation that happens at the interface of the swept-up material also creates the variable opacity needed to shield some of the wind material from ionising radiation, which then quickly recombines and allows the formation of molecules. Non ionising radiation leaks more readily because the opacity above 913 Å is lower. These photons produce florescence of H_2.

In Figure 4 we see two time snapshots towards the end of the simulation. In the first panel we see a set of approximately radial spikes, but 200 years later those straight and thin spikes evolve to thicker and sometimes curved ones. In the right column of Figure 4 two different parts of the nebula exhibit thinner and straighter spikes (top-right panel) or thicker, bent ones (bottom-right panel). Although the entire nebula was ejected and ionized over a short time interval, there can be a delay in the evolution of a given spike in a specific part of the nebula, related to the local opacity in the swept-up shell. Figure 4 suggests that differences of only $\sim$ 200 years in the timescales of mass ejection and/or the progress of illumination along specific directions can explain the marked differences observed in the flocculent structure around the nebula.

The successful modelling of illumination percolating unevenly into the molecular halo (Figure 4) motivated a further geometric model of the halo, presented in Figure 5. This Figure compares the extended H_2 structures as imaged by JWST with a model consisting of two thick, concentric, unbroken but clumpy, shells of material that are illuminated by the central star through a porous ellipsoid representing the boundary of the ionised cavity, with reduced opacity in the polar regions. As a result of the uneven illumination the distribution of H_2 material appears fragmented and is generally brighter toward the polar regions (and suppressed along the equatorial plane) of the central ellipsoidal, ionised region. The distribution seen in the JWST H_2 images could be reproduced more closely by altering the opacity of the inner ellipsoid. Fly-though movies of the 3D reconstructions of both the inner ellipsoid (Figures 3) and the outer H_2 halo (Figure 5) can be found following the links.

The arches in the JWST images, are not smeared as is typical of those seen in projection [e.g., 50], but are instead sharp. This possibly indicates that these arches are on or near the plane of the sky, indicating that the orbit of the companion at $\sim$40-60 AU is closely aligned to the waist of the inner ellipsoid. This companion cannot partake in the formation of the disk around the central star, though it may play a secondary role in the shaping of other PN structures. It is also unlikely to have launched strong jets because at such distance the accretion rate would be very low. As such, this would be an additional companion to the inner binary (or triple), making it a tertiary (or quaternary) companion.

The visual A-type companion would then be a fourth (fifth) member of the group, an almost complete bystander from the point of view of interaction and shaping, but critically important for this study: Its well measured

mass, and slight evolved status, constrained the initial mass of the central star: (2.86±0.06) $M_{\odot}$.

To reconstruct the events that lead to the demise of the progenitor of NGC3132, the PN acts like a murder scene. The A-type companion, could not have partaken to the interaction that unravelled the AGB star, but was (and is) certainly present. A second companion at 40-60AU left an indelible trail of its presence in the form of arcs, but was not close enough to generate the dusty disk, nor shape the ionised cavity, implying that there must have been at least another accomplice. This points the finger at a close-by companion, that is either avoiding detection, or has perished in the interaction (merged). If the numerous protuberances seen in the ionised cavity come in pairs, then tumbling jet axes would be needed and this would point the finger to the presence of a *second*, close companion [47, 48], which would make the system a quintet. Even ignoring the putative second, close companion, we can state with good degree of certainty that the system is at least a quartet. Systems of four or five stars orbiting within a few ×1000 AU are not impossibly rare for primary stars in the progenitor mass range of interest here [e.g., HD 104237; 51]; indeed, present estimates indicate that 50% or more of stars of 2-3 $M_{\odot}$ are in multiple systems, and of order 2% of A-type stars have four companions [52].

JWST is at the starting gate of its promise as an astrophysical pathfinder. With complementary radio, interferometric and time resolved observations, it can find the temporal signatures of active convective mass ejection from the surfaces of AGB stars and the subsequent gravitational influence of companion stars in dynamically- and thermally-complex outflows. Thus JWST offers the potential to intimately connect the histories of PNe and the role of close stellar companions to studies of chemical evolution, nebular shaping and binary interactions for the next century.

Methods

Properties and distance of NGC 3132

The inner, ionised cavity of NGC 3132 is elliptical in shape, with a major axis of ∼40 arcsec (0.15 pc) and an electron density of $n \sim 10^3\,\mathrm{cm}^{-3}$. The ionization structure and abundances were the subject of a recent study by [53]. The nebula is also known to be molecule-rich [20]; it is among the brightest PNe in near-IR H_2 emission [21, 54].

A bright A2 V star is found near the centre of the PN, but is too cool to be the ionizing star; the actual PN progenitor is much fainter and is located ∼1.7 arcsec to the South-West of the A star [55, 56]. The A2 V star has the same radial velocity and extinction as the PN, and its proper motion ($\mu_\alpha = -7.747$ mas/yr $\sigma_{\mu_\alpha} = 0.026$; and $\mu_\delta = -0.125$ mas/yr $\sigma_{\mu_\delta} = 0.031$) agrees with that of the central star ($\mu_\alpha = -7.677$ mas/yr $\sigma_{\mu_\alpha} = 0.235$; and $\mu_\delta = 0.197$ mas/yr $\sigma_{\mu_\delta} = 0.275$), demonstrating that the PN progenitor and A-type companion constitute a comoving visual binary. The distance to NGC 3132 is obtained

from Gaia DR3 measurements of this visual binary. No Gaia DR3 radial velocity is available for the optically faint central star (the PN progenitor). However, the brighter (A-type) visual companion and the PN have the same radial velocity: (-11.4 ± 1.6) km s^{-1} for the A star from Gaia, and (-10 ± 3) km s^{-1} for the PN from [57]. The A star and PN central star also have compatible Gaia DR3 proper motions (within 1.5σ).

The brighter, A-type star has a Gaia DR3 geometric distance (median of geometric distance posterior) of 754 pc, with lower and upper 1σ-like confidence intervals (16th and 87th percentiles of the posterior) of 18 pc and 15 pc respectively [58]. The fainter central star has a Gaia DR3 geometric distance of 2124.7 pc, with lower and upper 1σ-like bars of 559.1 pc, and 1464.5 pc. The quality flags of the astrometric solution for this star are not optimal, most likely due to the vicinity of the much brighter A-star; in particular, the goodness-of-fit along the scan is 16.9, while it should be close to unity. We therefore adopt the Gaia DR3 distance to the central star's visual A-type companion, 754^{+15}_{-18} pc, as the distance to the PN.

Densities, masses and excitation of the H_2 knots

The clumpiness of NGC 3132 in H_2 emission links this nebula to other molecule-rich PNe, such as the Helix Nebula (NGC 7293, [59–62]), Ring Nebula (NGC 6720, [63]), and the hourglass-shaped (bipolar) nebula NGC 2346 [64], in which the molecular emission seems to be associated with dense knots that are embedded in or surround the ionised gas. The origin of such H_2 knots in PNe — as overdensities in the former AGB wind, vs. formation *in situ* following recombination of H, as the central star enters the cooling track — remains an open question [65]. In contrast to the Helix Nebula, there is little evidence for cometary tails emanating from the knots in the inner regions of NGC 3132. However, NGC 3132's system of approximately radially-directed H_2 spikes external to the main H_2-bright ring system has close analogues in, e.g., the Ring and Dumbbell Nebulae [21, 63].

Some H_2 knots in NGC 3132 are seen in absorption against the bright background nebular emission. This extinction is apparent not only in optical (HST) images but also, surprisingly, even in the JWST NIRCam near-infrared images (see Supplementary Figure 4). We measured the extinction at 1.87 μm for two knots seen in absorption against the (Paα) nebula background: the largest knot on the west side (coordinates 10:07:00.4, −40:26:08.8), and one of the darkest on the east side (10:07:02.5, −40:26:00.3). The diameters of these knots are ∼0.36 arcsec and ∼0.15 arcsec, while their extinction is ∼0.57 mag and ∼0.25 mag (at 1.87 μm), respectively; using the dust extinction law $A(\lambda)/A(V)$ from [66], the corresponding values of $A(V)$ are 3.9 and 1.7 mag assuming $R_V = 3.1$. We then estimate the hydrogen column densities $N(\mathrm{H})$ from these extinction measurements, and convert to the hydrogen density $n(\mathrm{H})$ of the knot by assuming that the knot diameters are roughly equivalent to their depths along the line of sight. Using the conversion between $A(V)$ and $N(\mathrm{H})$ from [67], where H is the combination of H^0, H^+ and H_2, the estimated column densities

are $N(\mathrm{H}) = 7.3 \times 10^{21}\,\mathrm{cm}^{-2}$ and $N(\mathrm{H}) = 3.2 \times 10^{21}\,\mathrm{cm}^{-2}$, respectively. For the adopted distance of 754 pc, the estimated densities are $n(\mathrm{H}) \sim 2 \times 10^{6}\,\mathrm{cm}^{-3}$ for both knots. These densities suggest knot masses of $10^{-5}\,\mathrm{M}_{\odot}$, similar to the typical knot ("globule") masses found in the Helix Nebula [68].

The critical density of excitation of the 2.12 μm H_2 1–0 S(1) line at a kinetic temperature of 2000 K is $9{\times}10^{5}\,\mathrm{cm}^{-3}$ [69], if the collision partner is H. The critical density is higher for the 1–0 S(1) line than for the 0–0 S(9) 4.69 μm H_2 line [$6{\times}10^{4}$ cm^{-3}; 69, 70]. Hence, the excitation of H_2 should be nearly thermal if the gas temperature is sufficiently high, with the caveat that both critical densities are higher if the primary collision partner is H_2 rather than H.

PSF measurements of the central star

To ascertain whether the mid-IR source associated with the PN central star is extended, we measured the JWST instrumental point spread function (PSF), using Gaussian fitting of field stars. We measured Gaussian FWHMs of 0.29, 0.40, 0.44 and 0.58 arcsec at 7.7, 11.3, 12.8 and 18 μm, respectively. We also measured two compact, slightly resolved galaxies in the field.

We then repeated the procedure for the central star. No fit was possible at 18 μm, due to saturation (see Supplementary Figure 5). At 7.7 μm the central star is on the edge of the diffraction spike of the A star, and only an upper limit on FWHM could be obtained. However, measurements of the PN central star image in the 11.3 and 12.8 μm filters gave consistent results, with measured FWHMs of 0.55 and 0.60 arcsec, significantly larger than the respective PSFs and comparable to the two field galaxies. Gaussian deconvolution using the PSF yields deconvolved FWHM values for the central star of ≤ 0.3 (≤ 230 AU) at 7 μm, and 0.4 arcsec (300 AU) at 11.3 and 12.8 μm. The extent of the central star at 18 μm is $\gtrsim 0.9$ arcsec in diameter (see Supplemenraty Figures 5 and 7).

Central star system's masses

We determined the mass of the A-star companion using version 1.2 of the PARSEC isochrones [71] for solar metallicity, taken as $Z = 0.0152$. We used $M_{\mathrm{bol},0} = (0.34 \pm 0.25)$ mag and the GAIA DR3 spectroscopic temperature $T_{\mathrm{eff}} = (9200 \pm 200)$ K, where the errors are conservative. The star is confirmed to be beginning to turn off the main sequence, in a phase where the luminosity of $(57 \pm 15)\,\mathrm{L}_{\odot}$ increases by 0.1% per Myr and the temperature decreases by 7 K per Myr (see Supplementary Figure 6). The isochrones yield an age of $(5.3 \pm 0.3) \times 10^{8}$ yr and a mass of $M_{\mathrm{A2V}} = (2.40 \pm 0.15)\,\mathrm{M}_{\odot}$. The central star of the PN is evolving on the same isochrone, but from a more massive star as it has evolved further. We use the same isochrones to determine the initial mass of a star on the thermal-pulsing AGB, the phase where the central star ejected the envelope. This gives an initial mass for the central star of $M_{\mathrm{i}} = (2.86{\pm}0.06)\,\mathrm{M}_{\odot}$. We have carried out the same isochrone fitting using an alternative stellar evolutionary model (the DARTMOUTH code; [72]). Both

the A2V star mass and the mass of the progenitor of the central star decrease by 0.15 $M_\odot$.

The final, CS, mass for such a star is 0.66 $M_\odot$. However, we have shown that such a star would show a high C/O$\sim$2, while the presence of silicate features in the Spitzer spectrum indicate that C/O$\lesssim$1. To reconcile the mass and the abundances we conjecture that the evolution was interrupted by the binary interaction that formed the disk, when the core mass was 0.61 $M_\odot$. With such a mass the evolutionary time to the current position on the HR diagram is in better agreement with the age of the nebula. This mass is also in better agreement with that derived from the photoionisation model (0.58$\pm$0.03) $M_\odot$.

Photoionisation modelling

The stratified ionisation and excitation structure of NGC 3132 is evident in Fig. 1, wherein the bright rim of ionized gas, as traced by [S III] and Brα emission, lies nestled inside the peak H_2 emission. However, significant ionised hydrogen and high-excitation plasma — traced by [Ne II] and [S III] emission in the MIRI F1280W and F1800W filter images, respectively — is observed beyond the bright inner, elliptical ring.

We constructed a three-dimensional photoionisation model using the code Mocassin [73]. To constrain the model we used the Multi Unit Spectroscopic Explorer (MUSE) emission line maps and absolute Hβ flux of [74], the optical integrated line fluxes from [75], the IR line fluxes from [76], as well as the velocity-position data obtained from the high-resolution scanning Fabry-Perot interferometer, SAM-FP, mounted on the SOAR telescope adaptive module. The observations were taken under photometric conditions. The seeing during the observations was 0.7 arcsec for the [N II] observations to 0.9 arcsec for the Hα one. The FWHM of a Ne calibration lamp lines was 0.586 Å or 26.8 km s^{-1}, which corresponds to a spectral resolution of about 11 200 at Hα.

We determined the density structure by fitting the emission line maps to the SAM-FP images of [N II] λ6584 and Hα, using a distance of 754 kpc. The model adopts as free parameters the temperature and luminosity of the ionising source, and the elemental abundance of the gas component (assumed constant throughout the nebula); we assumed that no dust is mixed in the gas. For the ionising source we use the NLTE model atmospheres of central stars of planetary nebulae from [77].

We find that a model invoking an unobscured central star with effective temperature $T_{\rm eff}$ = 110 kK and luminosity L = 200 $L_\odot$ well matches the observational data. However, we find that the present-day central star mass implied by the comparison, between these stellar parameters and the evolutionary tracks of [40] (0.58 $\pm$ 0.03 $M_\odot$) is inconsistent with the (large) initial mass inferred from consideration of the presence of the comoving, wide-separation A-type companion (0.66 $M_\odot$; see Central star system's masses). Furthermore, the tracks of [40] indicate that, for this mass, we would have a post-AGB age of 20 000 yrs, whereas the position-velocity data from the SAM-FP instrument

yield an expansion velocity of 25-35 km s^{-1} implying a much shorter and inconsistent nebular dynamical age in the range 2200–5700 yrs.

The C/O and N/O abundances of the nebula, as well as the crystalline silicate nature of the dust in the PN, indicate that this object has not undergone hot bottom burning *and* that it has not undergone sufficient dredge up to have increased the C/O ratio above unity. By the time the 2.86-$M_\odot$ star reaches the tip of the AGB its C/O ratio is approximately 2. It therefore seems that the mass implied by the initial-to-final mass relation using a main sequence mass of 2.86 $M_\odot$, is too high. We have two ways to resolve this inconsistency (which may both be operating). The central star is shielded by dust in the circumstellar disk making it appear, to the PN, as a cooler star, and/or the central star mass is actually smaller than 0.66 $M_\odot$, because the AGB evolution was interrupted by a binary interaction.

If the stellar ascent of the AGB was interrupted, we can determine the upper limit for a mass that would produce a nebula with $C/O \lesssim 1$ and N/O$\sim$0.4. This is 0.61 $M_\odot$. The time for a star of this mass to move from the AGB to the location on the HR diagram with an approximate temperature and luminosity (110kK, 200 $L_\odot$) as measured above is $\sim$10 000 yrs. The time-scale of the transition from AGB to post-AGB and PN is tightly connected with the rate at which the envelope is consumed: the results obtained are therefore sensitive to the mass-loss description. The time of 10 000 yr, is based on the classic mass loss rates dictated by Reimers or Blocker [78]. This estimate must be considered as an upper limit of the duration of this phase; indeed the recent works on the AGB to post-AGB transition by [79] and [80] showed that to reproduce the infrared excess of post-AGB stars in the Galaxy and in the Magellanic Clouds one has to invoke significantly higher mass-loss rates than those based on the aforementioned formulations, something that would reduce the time-scales by a factor of $\sim$5. The timescale of 10 000 yrs is therefore easily reconciled with the observed timescale of 2200-5700 yrs implied by the nebula.

Hydrodynamic modelling

The hydrodynamic simulation used to interpret the fragmentation and radial spikes is a 2-dimensional hydrodynamic simulation using the magneto-hydrodynamic code ZEUS-3D. The computational grid is in spherical coordinates and consists of 800 $\times$ 800 equidistant zones in r and θ respectively, with an angular extent of 90°. The wind and UV luminosity inputs correspond to a stellar post-AGB model with 0.677 $M_\odot$ which evolves from an initial 2.5 $M_\odot$ main sequence star [81].

At simulation time 0 yr the star has $T_{\rm eff}$ = 10 000 K and the AGB wind (v = 10 km s^{-1}, $\dot{M} = 10^{-6}$ $M_\odot$ yr^{-1}) has a homogeneous distribution outside of the pre-PN. The pre-PN has had 1000 yr of evolution prior to this moment, during which time a wide magnetic jet operated with a velocity v = 230 km s^{-1}, and a mass-loss rate $\dot{M} = 1.3 \times 10^{-7}$ $M_\odot$ yr^{-1}; this simulation is taken from Model C6 in [82]. At this time the star starts emitting a fast tenuous wind with a velocity v from 240 to 14 000 km s^{-1} and a mass-loss rate, $\dot{M}$ ranging

from 1.06×10^{-7} to 1.13×10^{-10} $M_{\odot}$ yr^{-1} over 4000 yrs that sweeps up the AGB wind material. At the same time (0 yr) the ionisation front propagates into the medium.

Data availability

HST data are available at *HST* Legacy Archive (https://hla.stsci.edu). JWST data were obtained from the Mikulski Archive for Space Telescopes at the Space Telescope Science Institute (https://archive.stsci.edu/). MUSE data were collected at the European Organisation for Astronomical Research in the Southern Hemisphere, Chile (ESO Programme 60.A-9100), presented by Monreal-Ibero et al. (2020) are available at the ESO Archive (http://archive.eso.org). San Pedro de Martir data is available at http://kincatpn.astrosen.unam.mx.

Code availability

The code MOCASSIN is available at the following URL: https://mocassin.nebulousresearch.org/. ZEUS3-D is available at the Laboratory for Computational Astrophysics [83]). The compiled version of *Shape* is available at http://www.astrosen.unam.mx/shape.

Acknowledgements. We would like to start by acknowledging the International Astronomical Union that oversees the work of Commission H3 on Planetary Nebulae. It is through the coordinating activity of this committee that this paper came together. SA acknowledges support under the grant 5077 financed by IAASARS/NOA. JA and VB acknowledge support from EVENTs/NEBULAE WEB research program, Spanish AEI grant PID2019-105203GB-C21. IA acknowledges the support of CAPES, Brazil (Finance Code 001). EDB acknowledges financial support from the Swedish National Space Agency. EB acknowledges NSF grants AST-1813298 and PHY-2020249. JC and EP acknowledge support from an NSERC Discovery Grant. GG-S thanks Michael L. Norman and the Laboratory for Computational Astrophysics for the use of ZEUS-3D. DAGH and AM acknowledge support from the ACIISI, Gobierno de Canarias and the European Regional Development Fund (ERDF) under grant with reference PROID2020010051 as well as from the State Research Agency (AEI) of the Spanish Ministry of Science and Innovation (MICINN) under grant PID2020-115758GB-I00. JGR acknowledges support from Spanish AEI under Severo Ochoa Centres of Excellence Programme 2020-2023 (CEX2019-000920-S). JGR and VGLL acknowledge support from ACIISI and ERDF under grant ProID2021010074. DGR acknowledges the CNPq grant 313016/2020-8. MAG acknowledges support of grant PGC 2018-102184-B-I00 of the Ministerio de Educación, Innovación y Universidades cofunded with FEDER funds and from the State Agency for Research of the Spanish MCIU through the "Center of Excellence Severo Ochoa" award to the Instituto de Astrofísica de Andalucía (SEV-2017-0709).

DJ acknowledges support from the Erasmus+ programme of the European Union under grant number 2020-1-CZ01-KA203-078200. AK and ZO were supported by the Australian Research Council Centre of Excellence for All Sky Astrophysics in 3 Dimensions (ASTRO 3D), through project number CE170100013. This research is/was supported by an Australian Government Research Training Program (RTP) Scholarship. MM and RW acknowledge support from STFC Consolidated grant (2422911). CM acknowledges support from UNAM/DGAPA/PAPIIT under grant IN101220. SM acknowledges funding from UMiami, the South African National Research Foundation and the University of Cape Town VC2030 Future Leaders Award. JN acknowledges support from NSF grant AST-2009713. CMdO acknowledges funding from FAPESP through projects 2017/50277-0, 2019/11910-4 e 2019/26492-3 and CNPq, process number 309209/2019-6. JHK and PMB acknowledge support from NSF grant AST-2206033 and a NRAO Student Observing Support grant to Rochester Institute of Technology. MO was supported by JSPS Grants-in-Aid for Scientific Research(C) (JP19K03914 and 22K03675).

QAP acknowledges support from the HKSAR Research grants council. Vera C. Rubin Observatory is a Federal project jointly funded by the National Science Foundation (NSF) and the Department of Energy (DOE) Office of Science, with early construction funding received from private donations through the LSST Corporation. The NSF-funded LSST (now Rubin Observatory) Project Office for construction was established as an operating center under the management of the Association of Universities for Research in Astronomy (AURA). The DOE-funded effort to build the Rubin Observatory LSST Camera (LSSTCam) is managed by SLAC National Accelerator Laboratory (SLAC).

AJR was supported by the Australian Research Council through award number FT170100243. LS acknowledges support from PAPIIT UNAM grant IN110122. CSC's work is part of I+D+i project PID2019-105203GB-C22 funded by the Spanish MCIN/AEI/10.13039/501100011033. MSG acknowledges support by the Spanish Ministry of Science and Innovation (MICINN) through projects AxIN (grant AYA2016-78994-P) and EVENTs/Nebulae-Web (grant PID2019-105203GB-C21). RS's contribution to the research described here was carried out at the Jet Propulsion Laboratory, California Institute of Technology, under a contract with NASA. J.A.T. would like to thank Marcos Moshisnky Fundation (Mexico) and UNAM PAPIIT project IA101622 EV acknowledges support from the "On the rocks II project" funded by the Spanish Ministerio de Ciencia, Innovación y Universidades under grant PGC2018-101950-B-I00. AZ acknowledges support from STFC under grant ST/T000414/1.

This research made use of Photutils, an Astropy package for detection and photometry of astronomical sources [84], of the Spanish Virtual Observatory (https://svo.cab.inta-csic.es) project funded by MCIN/AEI/10.13039/501100011033/ through grant PID2020-112949GB-I00 and of the computing facilities available at the Laboratory of Computational

Astrophysics of the Universidade Federal de Itajubá (LAC-UNIFEI, which is maintained with grants from CAPES, CNPq and FAPEMIG).

Based on observations made with the NASA/ESA Hubble Space Telescope, and obtained from the Hubble Legacy Archive, which is a collaboration between the Space Telescope Science Institute (STScI/NASA), the Space Telescope European Coordinating Facility (ST-ECF/ESAC/ESA) and the Canadian Astronomy Data Centre (CADC/NRC/CSA).

The JWST Early Release Observations and associated materials were developed, executed, and compiled by the ERO production team: Hannah Braun, Claire Blome, Matthew Brown, Margaret Carruthers, Dan Coe, Joseph DePasquale, Nestor Espinoza, Macarena Garcia Marin, Karl Gordon, Alaina Henry, Leah Hustak, Andi James, Ann Jenkins, Anton Koekemoer, Stephanie LaMassa, David Law, Alexandra Lockwood, Amaya Moro-Martin, Susan Mullally, Alyssa Pagan, Dani Player, Klaus Pontoppidan, Charles Proffitt, Christine Pulliam, Leah Ramsay, Swara Ravindranath, Neill Reid, Massimo Robberto, Elena Sabbi, Leonardo Ubeda. The EROs were also made possible by the foundational efforts and support from the JWST instruments, STScI planning and scheduling, and Data Management teams.

Finally, this work would not have been possible without the collaborative platforms *Slack* (slack.com) and *Overleaf* (overleaf.com).

Author contribution

The following authors have contributed majorly to multiple aspects of the work that lead to this paper, the writing and the formatting of figures: De Marco (writing, structure, interpretation, synthesis), Aleman (H_2 interpretation), Balick (processing and interpreting images), García-Segura (2D hydro modelling), Kastner (writing, H_2 measurements and interpretation), Matsuura (imaging, photometry, H_2 interpretation), Miszalski (stellar photometry), Mohamed (hydrodynamics of binaries), Monreal-Ibero (MUSE data analysis), Monteiro (photoionisation and morpho-kinematic models), Moraga Baez (JWST image production), Morisset (photoionisation modelling), Sahai (disk model, comparative interpretation), Soker (hydro modelling, interpretation), Stanghellini (distances, abundance interpretation), Steffen (morpho-kinematic models), Walsh (spatially resolved spectroscopy), Zijlstra (disk model, H_2 measurements, writing, interpretation).

The following authors have contributed key expertise to aspects of this paper: Akashi (hydrodynamic modelling and jet interpretation), Alcolea (CO observations), Akras (H_2 interpretation), Amram (space-resolved spectroscopy), Blackman (hydrodynamics), Bublitz (HST and radio images of fast evolving PN), Bucciarelli (*Gaia* data), Bujarrabal (radio observations,

disk observation and interpretation, comparative studies), Chu (disk interpretation), Cami (molecular formation), Corradi (final review, interpretation), García-Hernandez (IR dust/PAH features and abundances), García-Rojas (photoionisation modelling), Gómez-Llanos (photoionisation modelling), Gonçalves (comparative analysis), Guerrero (Xray imaging), Jones (close binaries), Karakas (final review, stellar nucleosynthesis), Manchado (nebular morphology, H_2 interpretation), McDonald (photometry modelling), Montez (X-ray and UV imaging), Osborn (binary nucleosynthesis), Otsuka (IR imaging), Parker (morphology), Peeters (nebular spectroscopy, PAHs), Ruiter (binary populations), Sabin (abundances), Sánchez Contreras (radio), Santander-García (nebular evolution), Seitenzahl (star and star nebula association), Speck (dust), Toalá (morphology), Ueta (nebular imaging), Van de Steene (IR observations), Ventura (AGB evolution model).

The following authors contributed by commenting on some aspects of the analysis and manuscript: De Beck, Boffin, Boumis, Chornay, Frank, Kwok, Lykou, Nordhaus, Oliveira, Quint, Quintana-Lacaci, Redman, Villaver, Vlemmings, Wesson, and Van Winckel.

Competing interest statement

We declare that no conflict of interest exists between any of the authors and the content and production of this paper.

Figures

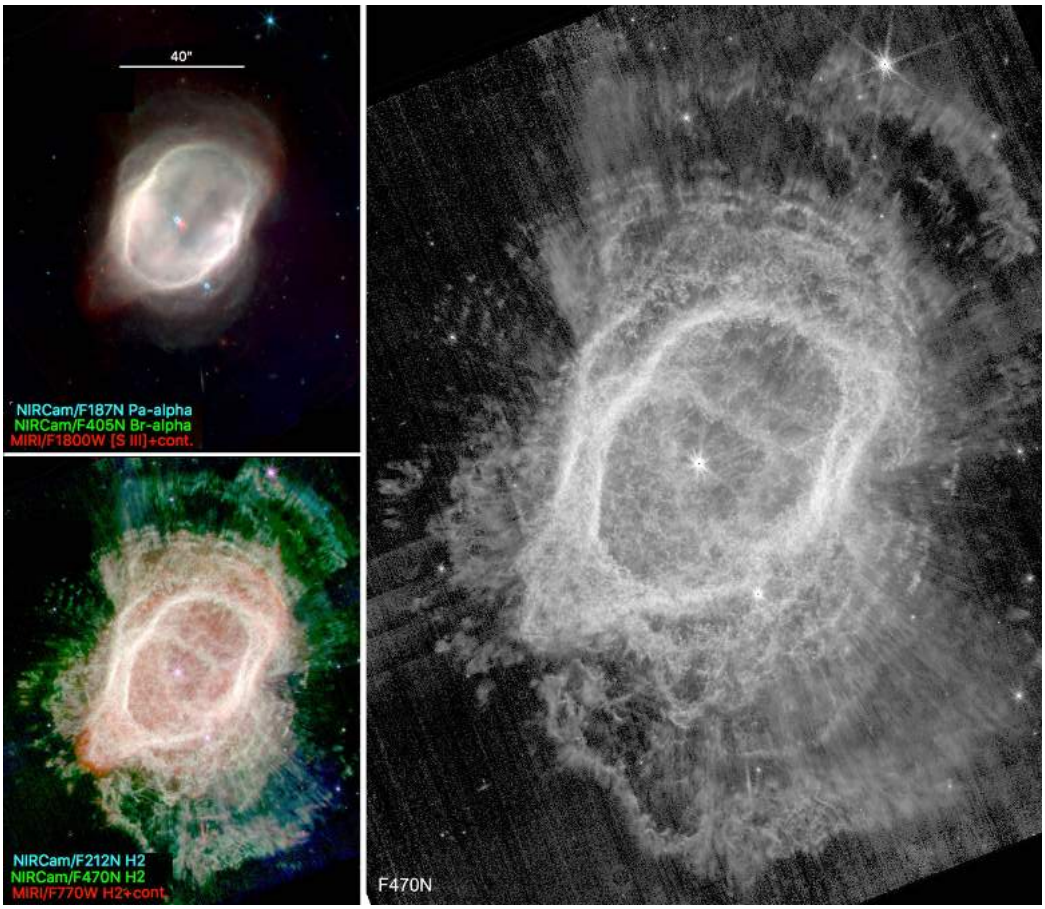

Fig. 1 JWST images of the PN NGC 3132. Left column, top and bottom: color overlays of JWST NIRCam and MIRI images that cleanly distinguish between the PN's ionized gas (i.e., H II region; top panel) and molecular gas (as seen in H_2; bottom panel). Note the sharp contrast between the relatively smooth appearance of the H II region and the flocculent structure of the H_2 ring system and extended H_2 halo. These images are presented with square-root and log intensity stretches, respectively, from the background sky to peak intensity levels in each image. Right image: a grey-scale, single filter (F470N), zoomed-in NIRCam image that more readily displays details of the flocculent H_2 halo. North is towards the top, East is towards the left.

References

[1] Mastrodemos, N. & Morris, M. Bipolar Pre-Planetary Nebulae: Hydrodynamics of Dusty Winds in Binary Systems. II. Morphology of the Circumstellar Envelopes. Astrophys. J. **523**, 357–380 (1999). https://doi.org/10.1086/307717 .

[2] Mohamed, S. & Podsiadlowski, P. Mass Transfer in Mira-type Binaries. Baltic Astronomy **21**, 88–96 (2012) .

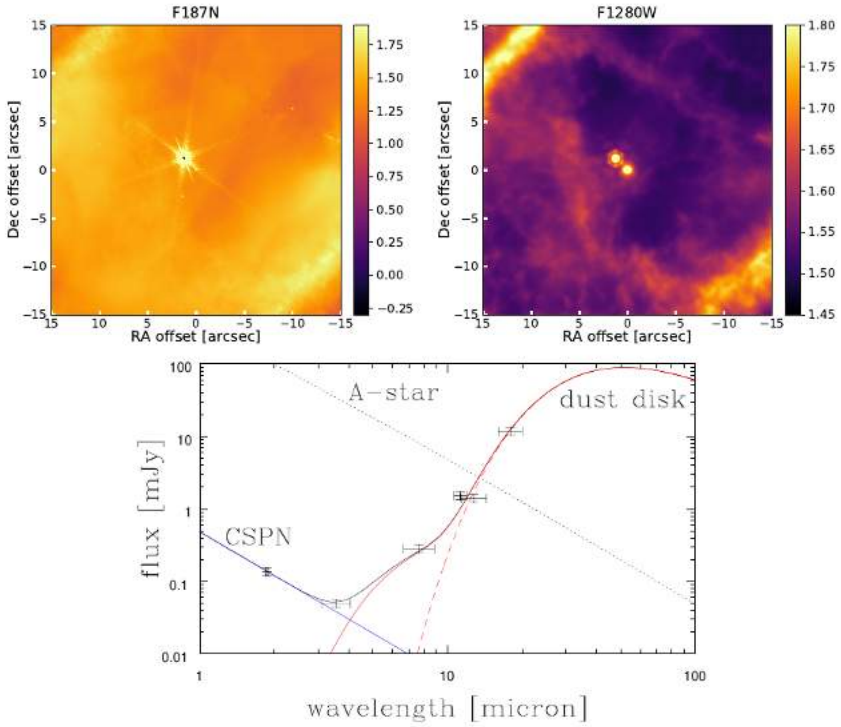

Fig. 2 The dusty central star of the PN NGC 3132. JWST NIRCam F187N (top left) and MIRI F1280W (top right) images of the central region of NGC 3132. The JWST MIRI images reveal the detection of a mid-IR excess at the nebula's true (hot, compact) central star, which is seen projected ∼1.7″ (∼1300AU) SW of the main-sequence A-type companion (which is far brighter shortward of ∼10 μm). North up and East is to the left. Colour bars indicate surface brightness in log (MJy ster^{-1}). The bottom panel shows the near-IR to mid-IR spectral energy distribution of the central star of NGC 3132 overlaid with a model consisting of a combination of a hot blackbody spectrum representing the central star's photosphere (blue line) and a dusty circumstellar double disk model to fit the NIR and MIR data points (red line, with the cooler disk as a dashed line). The wide companion, A star's spectral energy distribution is shown as a dotted line. Vertical error bars are set at 10% of the flux values, while horizzontal bars show the width of the bandpass.

[3] Maercker, M. et al. Unexpectedly large mass loss during the thermal pulse cycle of the red giant star R Sculptoris. Nature **490**, 232–234 (2012). https://doi.org/10.1038/nature11511, arXiv:1210.3030 [astro-ph.SR].

[4] Santander-García, M. et al. ALMA high spatial resolution observations of the dense molecular region of NGC 6302. Astron. Astrophys. **597**, A27 (2017). https://doi.org/10.1051/0004-6361/201629288, arXiv:1609.06455 [astro-ph.SR].

[5] Sahai, R. & Trauger, J. T. Multipolar Bubbles and Jets in Low-Excitation Planetary Nebulae: Toward a New Understanding of the Formation and Shaping of Planetary Nebulae. Astron. J. **116**, 1357–1366 (1998). https://doi.org/10.1086/300504 .

[6] Sahai, R., Morris, M. R. & Villar, G. G. Young Planetary Nebulae: Hubble

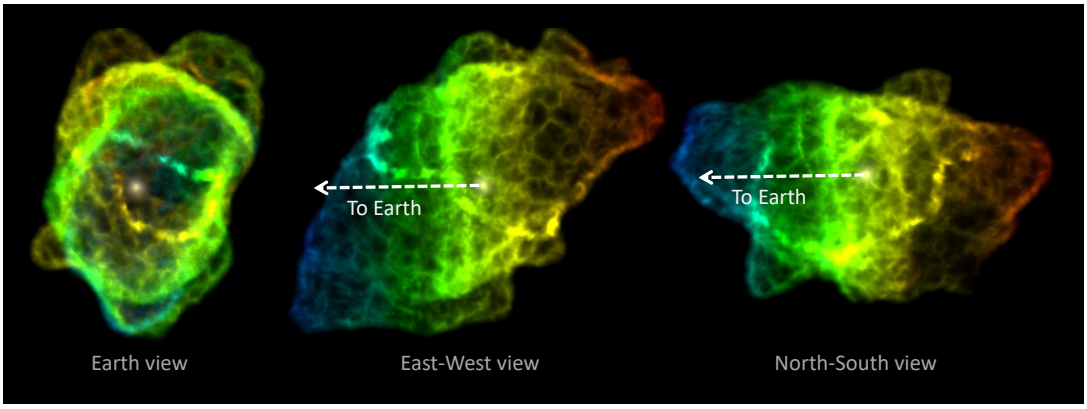

Fig. 3 Morpho-kinematic reconstruction of the ionised cavity of PN NGC 3132. Emission in the [N II] line as seen from Earth (left image; North is towards the top and East is towards the left), a view from the East, which we call East-West view (middle image), and a view from the North which we call North-South view (right image). The colour-coding is for Doppler-shift as seen from Earth, with blue for material approaching the observer, red for receding gas and green for no velocity along the observer's line of sight. We note the prominent green (zero Doppler shift) belt in the middle image, and the filament that wraps around the waist of the ellipsoid and which is red-shifted on one side and blue-shifted on the other. A fly-through movie of this model can be found at this link.

Space Telescope Imaging and a New Morphological Classification System. Astron. J. **141** (4), 134 (2011). https://doi.org/10.1088/0004-6256/141/4/134, arXiv:1101.2214 [astro-ph.GA].

[7] van Winckel, H. Post-Agb Stars. Annu. Rev. Astron. Astrophys. **41**, 391–427 (2003). https://doi.org/10.1146/annurev.astro.41.071601.170018 .

[8] Ivanova, N. et al. Common envelope evolution: where we stand and how we can move forward. Astron. Astrophys. Rev. **21**, 59 (2013). https://doi.org/10.1007/s00159-013-0059-2, arXiv:1209.4302 [astro-ph.HE].

[9] Mastrodemos, N. & Morris, M. Bipolar Preplanetary Nebulae: Hydrodynamics of Dusty Winds in Binary Systems. I. Formation of Accretion Disks. Astrophys. J. **497**, 303 (1998). https://doi.org/10.1086/305465 .

[10] Mohamed, S. & Podsiadlowski, P. R. Napiwotzki & M. R. Burleigh (ed.) Wind Roche-Lobe Overflow: a New Mass-Transfer Mode for Wide Binaries. (ed.R. Napiwotzki & M. R. Burleigh) 15th European Workshop on White Dwarfs, Vol. 372 of Astronomical Society of the Pacific Conference Series, 397 (2007).

[11] de Val-Borro, M., Karovska, M. & Sasselov, D. Numerical Simulations of Wind Accretion in Symbiotic Binaries. Astrophys. J. **700**, 1148–1160 (2009). https://doi.org/10.1088/0004-637X/700/2/1148, arXiv:0905.3542 [astro-ph.SR].

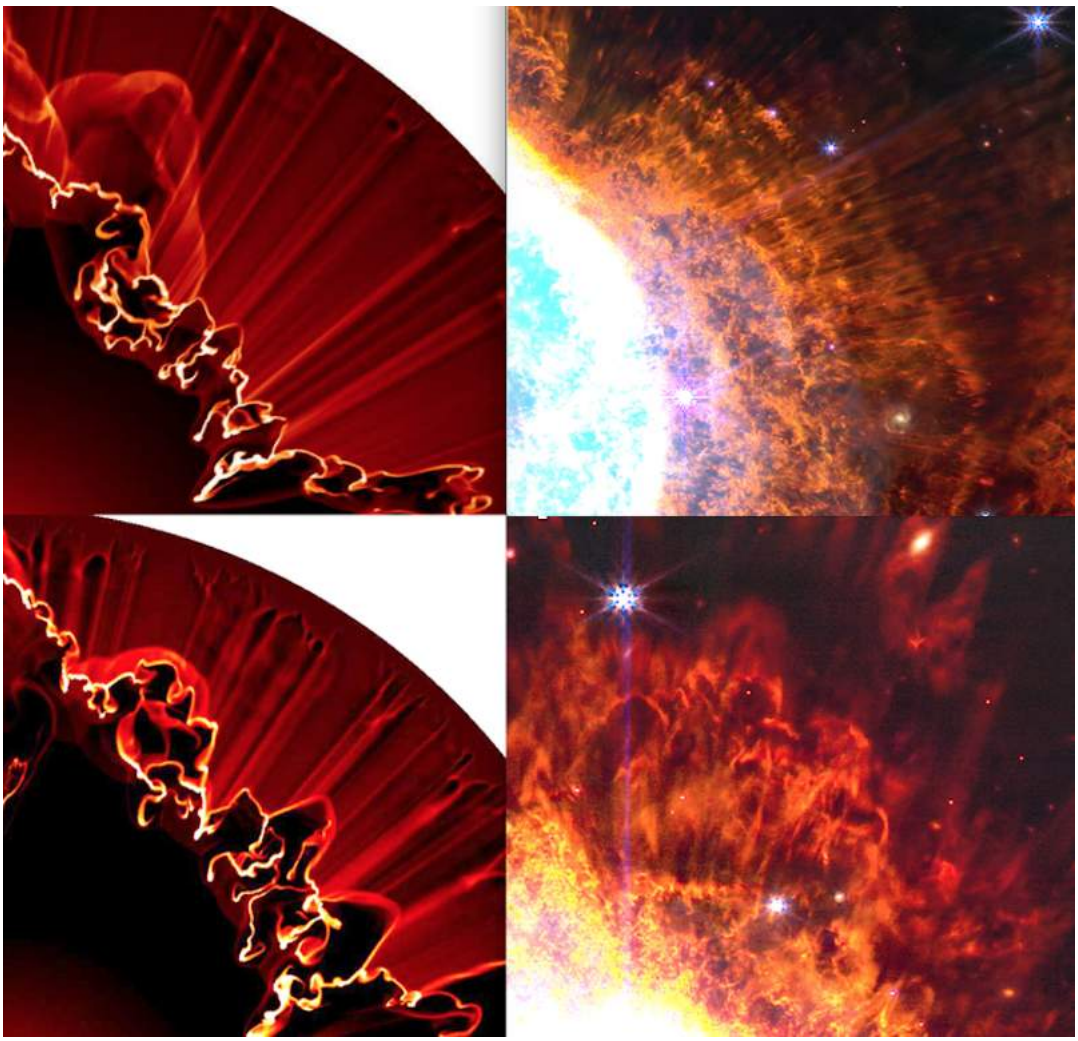

Fig. 4 The physical interpretation of the flocculent H_2 structure. Left column: a hydrodynamic simulation showing the formation of nebular structures external to the main ionised region, compared with (right column) two quadrants of the JWST images of NGC 3132. Top row: the simulation snapshot at 3800 yr from the on-set of ionisation is compared with similar straight spikes in one region of the nebula (top right image North is to the left, East is towards the top) while, bottom row, at 4000 yr the spikes thicken and bend as is also seen in a different part of the nebula (North to the top, and East to the left). This demonstrates temporal evolution in different parts of the nebula.

[12] Soker, N. Visual Wide Binaries and the Structure of Planetary Nebulae. Astron. J. **118** (5), 2424–2429 (1999). https://doi.org/10.1086/301090, arXiv:astro-ph/9907305 [astro-ph].

[13] Balick, B. et al. FLIERs and Other Microstructures in Planetary Nebulae. IV. Images of Elliptical PNs from the Hubble Space Telescope. Astron. J. **116**, 360–371 (1998). https://doi.org/10.1086/300429 .

[14] Sahai, R. & Trauger, J. T. Multipolar Bubbles and Jets in Low-Excitation Planetary Nebulae: Toward a New Understanding of the Formation and Shaping of Planetary Nebulae. Astron. J. **116** (3), 1357–1366 (1998).

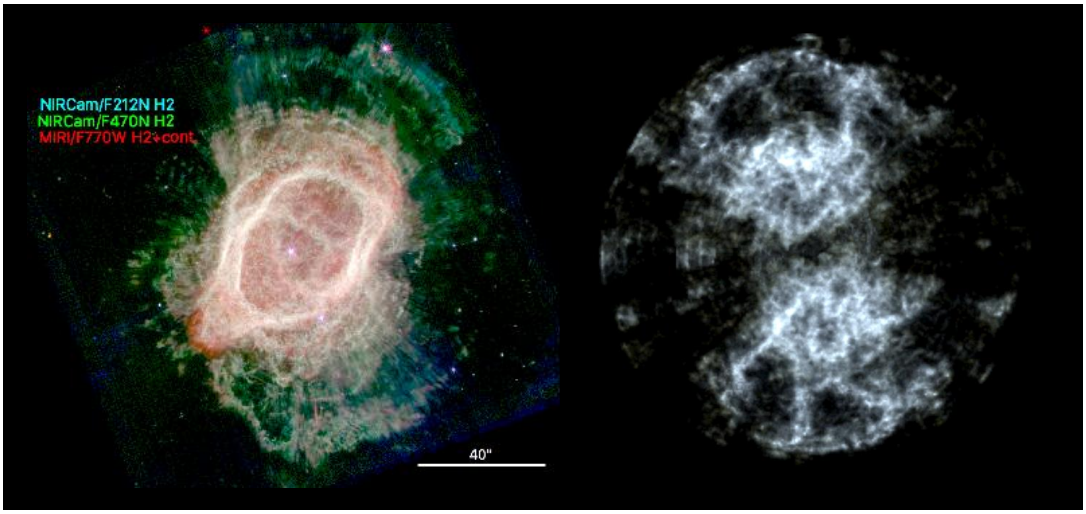

Fig. 5 Approximate illumination model of the H_2 halo of PN NGC 3132. Left panel: the JWST colour composite image showing the H_2 extended structure. Right panel the projected *Shape* image after assuming two concentric, thick uninterrupted shells of material, illuminated by the central star, through a porous ellipsoid with reduced opacity in the polar regions. Fly through movie of this model can be found at this link.

https://doi.org/10.1086/300504 .

[15] Sabbadin, F., Turatto, M., Ragazzoni, R., Cappellaro, E. & Benetti, S. The structure of planetary nebulae: theory vs. practice. Astron. Astrophys. **451** (3), 937–949 (2006). https://doi.org/10.1051/0004-6361:20054554, arXiv:astro-ph/0601283 [astro-ph].

[16] Steffen, W. & López, J. A. Morpho-Kinematic Modeling of Gaseous Nebulae with SHAPE. Revista Mexicana de Astronomía y Astrofísica **42**, 99–105 (2006). arXiv:astro-ph/0601585 .

[17] Balick, B. & Frank, A. Shapes and Shaping of Planetary Nebulae. Annu. Rev. Astron. Astrophys. **40**, 439–486 (2002). https://doi.org/10.1146/annurev.astro.40.060401.093849 .

[18] De Marco, O., Farihi, J. & Nordhaus, J. The WD perspective on the PN binary hypothesis. Journal of Physics Conference Series **172** (1), 012031–+ (2009). https://doi.org/10.1088/1742-6596/172/1/012031 .

[19] Jones, D. & Boffin, H. M. J. Binary stars as the key to understanding planetary nebulae. Nature Astronomy **1**, 0117 (2017). https://doi.org/10.1038/s41550-017-0117, arXiv:1705.00283 [astro-ph.SR].

[20] Sahai, R., Wootten, A. & Clegg, R. E. S. CO in the bipolar planetary nebula NGC 3132. Astron. Astrophys. **234**, L1–L4 (1990) .

[21] Kastner, J. H., Weintraub, D. A., Gatley, I., Merrill, K. M. & Probst, R. G. H_2 Emission from Planetary Nebulae: Signpost of Bipolar Structure.

Astrophys. J. **462**, 777 (1996). https://doi.org/10.1086/177192 .

[22] Abramovici, A. et al. LIGO: The Laser Interferometer Gravitational-Wave Observatory. Science **256** (5055), 325–333 (1992). https://doi.org/10.1126/science.256.5055.325 .

[23] Amaro-Seoane, P. et al. Laser Interferometer Space Antenna. arXiv e-prints arXiv:1702.00786 (2017). arXiv:1702.00786 [astro-ph.IM].

[24] Ivezic, Z. et al. Large Synoptic Survey Telescope: From Science Drivers To Reference Design. Serbian Astronomical Journal **176**, 1–13 (2008). https://doi.org/10.2298/SAJ0876001I .

[25] Santander-García, M. et al. The double-degenerate, super-Chandrasekhar nucleus of the planetary nebula Henize 2-428. Nature **519** (7541), 63–65 (2015). https://doi.org/10.1038/nature14124, arXiv:1609.00178 [astro-ph.SR].

[26] Chiotellis, A., Boumis, P. & Spetsieri, Z. T. The Interaction of Type Ia Supernovae with Planetary Nebulae: The Case of Kepler's Supernova Remnant. Galaxies **8** (2), 38 (2020). https://doi.org/10.3390/galaxies8020038, arXiv:2004.14493 [astro-ph.SR].

[27] Cikota, A., Patat, F., Cikota, S., Spyromilio, J. & Rau, G. Common continuum polarization properties: a possible link between proto-planetary nebulae and Type Ia Supernova progenitors. Mon. Not. R. Astron. Soc. **471** (2), 2111–2116 (2017). https://doi.org/10.1093/mnras/stx1734, arXiv:1707.02300 [astro-ph.SR].

[28] Hora, J. L. et al. Infrared Array Camera (IRAC) Observations of Planetary Nebulae. Astrophys. J. Suppl. Ser. **154** (1), 296–301 (2004). https://doi.org/10.1086/422820, arXiv:astro-ph/0405614 [astro-ph].

[29] Fang, X. et al. Extended Structures of Planetary Nebulae Detected in H_2 Emission. Astrophys. J. **859** (2), 92 (2018). https://doi.org/10.3847/1538-4357/aac01e, arXiv:1804.08840 [astro-ph.SR].

[30] Ramos-Larios, G. et al. Rings and arcs around evolved stars - I. Fingerprints of the last gasps in the formation process of planetary nebulae. Mon. Not. R. Astron. Soc. **462** (1), 610–635 (2016). https://doi.org/10.1093/mnras/stw1572 .

[31] Guerrero, M. A., Ramos-Larios, G., Toalá, J. A., Balick, B. & Sabin, L. Rings and arcs around evolved stars - II. The Carbon Star AFGL 3068 and the Planetary Nebulae NGC 6543, NGC 7009, and NGC 7027. Mon. Not. R. Astron. Soc. **495** (2), 2234–2246 (2020). https://doi.org/10.1093/mnras/staa1225, arXiv:2004.14040 [astro-ph.SR].

[32] Kim, H., Liu, S.-Y. & Taam, R. E. Templates of Binary-induced Spiral-shell Patterns around Mass-losing Post-main-sequence Stars. Astrophys. J. Suppl. Ser. **243** (2), 35 (2019). https://doi.org/10.3847/1538-4365/ab297e, arXiv:1906.06333 [astro-ph.SR].

[33] Maes, S. et al. SPH modelling of companion-perturbed AGB outflows including a new morphology classification scheme. Astron. Astrophys. **653**, A25 (2021). https://doi.org/10.1051/0004-6361/202140823, arXiv:2107.00505 [astro-ph.SR].

[34] Aydi, E. & Mohamed, S. 3D models of the circumstellar environments of evolved stars: Formation of multiple spiral structures. Mon. Not. R. Astron. Soc. **513** (3), 4405–4430 (2022). https://doi.org/10.1093/mnras/stac749, arXiv:2203.08318 [astro-ph.SR].

[35] Decin, L. et al. (Sub)stellar companions shape the winds of evolved stars. Science **369** (6510), 1497–1500 (2020). https://doi.org/10.1126/science.abb1229, arXiv:2009.11694 [astro-ph.SR].

[36] Méndez, R. H. A-type central stars of planetary nebulae - II. The central stars of NGC 2346, He 2-36 and NGC 3132. Mon. Not. R. Astron. Soc. **185**, 647–660 (1978) .

[37] Wright, E. L. et al. The Wide-field Infrared Survey Explorer (WISE): Mission Description and Initial On-orbit Performance. Astron. J. **140** (6), 1868–1881 (2010). https://doi.org/10.1088/0004-6256/140/6/1868, arXiv:1008.0031 [astro-ph.IM].

[38] Su, K. Y. L. et al. A Debris Disk around the Central Star of the Helix Nebula? Astrophys. J. Lett. **657**, L41–L45 (2007). https://doi.org/10.1086/513018, arXiv:astro-ph/0702296 .

[39] Clayton, G. C. et al. Dusty Disks around Central Stars of Planetary Nebulae. Astron. J. **147**, 142 (2014). https://doi.org/10.1088/0004-6256/147/6/142, arXiv:1403.5795 [astro-ph.SR].

[40] Ventura, P., Karakas, A., Dell'Agli, F., García-Hernández, D. A. & Guzman-Ramirez, L. Gas and dust from solar metallicity AGB stars. Mon. Not. R. Astron. Soc. **475** (2), 2282–2305 (2018). https://doi.org/10.1093/mnras/stx3338, arXiv:1712.08582 [astro-ph.SR].

[41] Huang, S.-S. Modes of Mass Ejection by Binary Stars and the Effect on Their Orbital Periods. Astrophys. J. **138**, 471 (1963). https://doi.org/10.1086/147659 .

[42] Soberman, G. E., Phinney, E. S. & van den Heuvel, E. P. J. Stability criteria for mass transfer in binary stellar evolution. Astron. Astrophys.

327, 620–635 (1997). astro-ph/9703016 .

[43] van Winckel, H. et al. Post-AGB stars with hot circumstellar dust: binarity of the low-amplitude pulsators. Astron. Astrophys. **505**, 1221–1232 (2009). https://doi.org/10.1051/0004-6361/200912332, arXiv:0906.4482 [astro-ph.SR].

[44] Sahai, R. The Starfish Twins: Two Young Planetary Nebulae with Extreme Multipolar Morphology. Astrophys. J. Lett. **537** (1), L43–L47 (2000). https://doi.org/10.1086/312748 .

[45] Akashi, M. & Soker, N. Shaping "Ears" in Planetary Nebulae by Early Jets. Astrophys. J. **913** (2), 91 (2021). https://doi.org/10.3847/1538-4357/abf7bb, arXiv:2012.08917 [astro-ph.GA].

[46] Bear, E. & Soker, N. Planetary Nebulae that Cannot Be Explained by Binary Systems. Astrophys. J. Lett. **837** (1), L10 (2017). https://doi.org/10.3847/2041-8213/aa611c, arXiv:1606.08149 [astro-ph.SR].

[47] Hamers, A. S., Glanz, H. & Neunteufel, P. A Statistical View of the Stable and Unstable Roche Lobe Overflow of a Tertiary Star onto the Inner Binary in Triple Systems. Astrophys. J. Suppl. Ser. **259** (1), 25 (2022). https://doi.org/10.3847/1538-4365/ac49e7, arXiv:2110.00024 [astro-ph.SR].

[48] Glanz, H. & Perets, H. B. Simulations of common envelope evolution in triple systems: circumstellar case. Mon. Not. R. Astron. Soc. **500** (2), 1921–1932 (2021). https://doi.org/10.1093/mnras/staa3242, arXiv:2004.00020 [astro-ph.SR].

[49] Höfner, S. & Olofsson, H. Mass loss of stars on the asymptotic giant branch. Mechanisms, models and measurements. Astron. Astrophys. Rev. **26** (1), 1 (2018). https://doi.org/10.1007/s00159-017-0106-5 .

[50] Balick, B. et al. The Illumination and Growth of CRL 2688: An Analysis of New and Archival Hubble Space Telescope Observations. Astrophys. J. **745** (2), 188 (2012). https://doi.org/10.1088/0004-637X/745/2/188, arXiv:1110.5678 [astro-ph.SR].

[51] Feigelson, E. D., Lawson, W. A. & Garmire, G. P. The ϵ Chamaeleontis Young Stellar Group and the Characterization of Sparse Stellar Clusters. Astrophys. J. **599** (2), 1207–1222 (2003). https://doi.org/10.1086/379365, arXiv:astro-ph/0309059 [astro-ph].

[52] Duchêne, G. & Kraus, A. Stellar Multiplicity. Annu. Rev. Astron. Astrophys. **51**, 269–310 (2013). https://doi.org/10.1146/annurev-astro-081710-102602, arXiv:1303.3028 [astro-ph.SR].

[53] Monreal-Ibero, A. & Walsh, J. R. The MUSE view of the planetary nebula NGC 3132. Astron. Astrophys. **634**, A47 (2020). https://doi.org/10.1051/0004-6361/201936845, arXiv:1912.02847 [astro-ph.SR].

[54] Storey, J. W. V. Molecular hydrogen observations of southern planetary nebulae. Mon. Not. R. Astron. Soc. **206**, 521–527 (1984). https://doi.org/10.1093/mnras/206.3.521 .

[55] Kohoutek, L. & Laustsen, S. Central star of NGC 3132: a visual binary. Astron. Astrophys. **61**, 761–763 (1977) .

[56] Ciardullo, R., Jacoby, G. H., Ford, H. C. & Neill, J. D. Planetary nebulae as standard candles. II - The calibration in M31 and its companions. Astrophys. J. **339**, 53–69 (1989). https://doi.org/10.1086/167275 .

[57] Meatheringham, S. J., Wood, P. R. & Faulkner, D. J. A study of some southern planetary nebulae. Astrophys. J. **334**, 862–874 (1988). https://doi.org/10.1086/166882 .

[58] Bailer-Jones, C. A. L., Rybizki, J., Fouesneau, M., Demleitner, M. & Andrae, R. Estimating Distances from Parallaxes. V. Geometric and Photogeometric Distances to 1.47 Billion Stars in Gaia Early Data Release 3. Astron. J. **161** (3), 147 (2021). https://doi.org/10.3847/1538-3881/abd806, arXiv:2012.05220 [astro-ph.SR].

[59] O'Dell, C. R., McCullough, P. R. & Meixner, M. Unraveling the Helix Nebula: Its Structure and Knots. Astron. J. **128** (5), 2339–2356 (2004). https://doi.org/10.1086/424621, arXiv:astro-ph/0407556 [astro-ph].

[60] Meixner, M., McCullough, P., Hartman, J., Son, M. & Speck, A. The Multitude of Molecular Hydrogen Knots in the Helix Nebula. Astron. J. **130** (4), 1784–1794 (2005). https://doi.org/10.1086/444539, arXiv:astro-ph/0509887 [astro-ph].

[61] Matsuura, M. et al. VLT/near-infrared integral field spectrometer observations of molecular hydrogen lines in the knots of the planetary nebula NGC 7293 (the Helix Nebula). Mon. Not. R. Astron. Soc. **382**, 1447–1459 (2007). https://doi.org/10.1111/j.1365-2966.2007.12496.x, arXiv:0709.3065 .

[62] Matsuura, M. et al. A "Firework" of H_2 Knots in the Planetary Nebula NGC 7293 (The Helix Nebula). Astrophys. J. **700** (2), 1067–1077 (2009). https://doi.org/10.1088/0004-637X/700/2/1067, arXiv:0906.2870 [astro-ph.SR].

[63] Kastner, J. H., Gatley, I., Merrill, K. M., Probst, R. & Weintraub, D. The Bipolar Symmetry of Ring-like Planetary Nebulae: Molecular Hydrogen

Emission from Halos. Astrophys. J. **421**, 600 (1994). https://doi.org/10.1086/173675 .

[64] Manchado, A. et al. High-resolution Imaging of NGC 2346 with GSAOI/GeMS: Disentangling the Planetary Nebula Molecular Structure to Understand Its Origin and Evolution. Astrophys. J. **808** (2), 115 (2015). https://doi.org/10.1088/0004-637X/808/2/115, arXiv:1506.03712 [astro-ph.SR].

[65] Fang, X. et al. Extended Structures of Planetary Nebulae Detected in H_2 Emission. Astrophys. J. **859** (2), 92 (2018). https://doi.org/10.3847/1538-4357/aac01e, arXiv:1804.08840 [astro-ph.SR].

[66] Cardelli, J. A., Clayton, G. C. & Mathis, J. S. The relationship between infrared, optical, and ultraviolet extinction. Astrophysical Journal **345**, 245 (1989). URL http://adsabs.harvard.edu/cgi-bin/nph-data_query?bibcode=1989ApJ...345..245C&link_type=ABSTRACT. https://doi.org/10.1086/167900 .

[67] Bohlin, R. C., Savage, B. D. & Drake, J. F. A survey of interstellar H I from L-alpha absorption measurements. II. Astrophysical Journal **224**, 132 (1978). URL http://adsabs.harvard.edu/cgi-bin/nph-data_query?bibcode=1978ApJ...224..132B&link_type=ABSTRACT. https://doi.org/10.1086/156357, a&AA ID. AAA022.131.015 .

[68] Andriantsaralaza, M., Zijlstra, A. & Avison, A. CO in the C1 globule of the Helix nebula with ALMA. Mon. Not. R. Astron. Soc. **491** (1), 758–772 (2020). https://doi.org/10.1093/mnras/stz3026, arXiv:1910.10982 [astro-ph.SR].

[69] Bourlot, J. L., Forêts, G. P. d. & Flower, D. R. The cooling of astrophysical media by H2. Monthly Notices of the Royal Astronomical Society **305** (4), 802–810 (1999). https://doi.org/10.1046/j.1365-8711.1999.02497.x .

[70] Wolniewicz, L., Simbotin, I. & Dalgarno, A. Quadrupole Transition Probabilities for the Excited Rovibrational States of H_2. Astrophys. J. Suppl. Ser. **115** (2), 293–313 (1998). https://doi.org/10.1086/313091 .

[71] Marigo, P. et al. A New Generation of PARSEC-COLIBRI Stellar Isochrones Including the TP-AGB Phase. Astrophys. J. **835** (1), 77 (2017). https://doi.org/10.3847/1538-4357/835/1/77, arXiv:1701.08510 [astro-ph.SR].

[72] Dotter, A. et al. The Dartmouth Stellar Evolution Database. Astrophys. J. Suppl. Ser. **178** (1), 89–101 (2008). https://doi.org/10.

1086/589654, arXiv:0804.4473 [astro-ph].

[73] Ercolano, B., Barlow, M. J., Storey, P. J. & Liu, X. W. MOCASSIN: a fully three-dimensional Monte Carlo photoionization code. Mon. Not. R. Astron. Soc. **340** (4), 1136–1152 (2003). https://doi.org/10.1046/j.1365-8711.2003.06371.x, arXiv:astro-ph/0209378 [astro-ph].

[74] Monreal-Ibero, A. & Walsh, J. R. The MUSE view of the planetary nebula NGC 3132. Astron. Astrophys. **634**, A47 (2020). https://doi.org/10.1051/0004-6361/201936845, arXiv:1912.02847 [astro-ph.SR].

[75] Tsamis, Y. G., Barlow, M. J., Liu, X.-W., Storey, P. J. & Danziger, I. J. A deep survey of heavy element lines in planetary nebulae - II. Recombination-line abundances and evidence for cold plasma. Mon. Not. R. Astron. Soc. **353**, 953–979 (2004). https://doi.org/10.1111/j.1365-2966.2004.08140.x, arXiv:astro-ph/0404280 .

[76] Mata, H. et al. Spitzer mid-infrared spectroscopic observations of planetary nebulae. Mon. Not. R. Astron. Soc. **459** (1), 841–853 (2016). https://doi.org/10.1093/mnras/stw646, arXiv:1603.06667 [astro-ph.SR].

[77] Rauch, T. NLTE spectral analysis of the sdOB primary of the eclipsing binary system LB 3459 (AA Dor). Astron. Astrophys. **356**, 665–675 (2000) .

[78] Blöcker, T. Stellar evolution of low- and intermediate-mass stars. II. Post-AGB evolution. Astron. Astrophys. **299**, 755 (1995) .

[79] Kamath, D. et al. New Post-AGB star models as tools to understand AGB evolution and nucleosynthesis. arXiv e-prints arXiv:2112.05535 (2021). arXiv:2112.05535 [astro-ph.SR].

[80] Tosi, S. et al. Understanding dust production and mass loss on the AGB phase using post-AGB stars in the Magellanic Clouds. arXiv e-prints arXiv:2208.08314 (2022). arXiv:2208.08314 [astro-ph.SR].

[81] Villaver, E., Manchado, A. & García-Segura, G. The Dynamical Evolution of the Circumstellar Gas around Low- and Intermediate-Mass Stars. II. The Planetary Nebula Formation. Astrophys. J. **581** (2), 1204–1224 (2002). https://doi.org/10.1086/344250, arXiv:astro-ph/0208323 [astro-ph].

[82] García-Segura, G., Taam, R. E. & Ricker, P. M. Common Envelope Shaping of Planetary Nebulae. III. The Launching of Jets in Proto-Planetary Nebulae. Astrophys. J. **914** (2), 111 (2021). https://doi.org/10.3847/1538-4357/abfc4e, arXiv:2104.12831 [astro-ph.SR].

[83] Clarke, D. A. A Consistent Method of Characteristics for Multidimensional Magnetohydrodynamics. Astrophys. J. **457**, 291 (1996). https://doi.org/10.1086/176730 .

[84] Bradley, L. et al. astropy/photutils:. Zenodo (2022).

arXiv:2301.02775v1 [astro-ph.SR] 7 Jan 2023

Supplementary Material

Specifications of JWST NIRCam and MIRI imaging

As part of its ERO program [1], JWST obtained ten images of NGC 3132: six individual NIRCam images, through filters F090W, F187N, F212N, F356W, F444W, and F470N, and four MIRI images, through filters F770W, F1130W, F1280W, F1800W (Supplementary Figure 1). Basic information about these NIRCam and MIRI filters is presented in Supplementary Table 1. The native NIRCam field of view is 2.2×2.2 arcmin, with a pixel scale of 0.031 arcsec/pixel in the range 0.6–2.3 μm and 0.063 arcsec/pixel in the range 2.4–5.0 μm; the native MIRI field of view is 1.7 × 1.3 arcmin with a pixel scale of 0.11 arcsec/pixel in the range 5-27 μm. The NIRCam instrument provides Nyquist-sampled imaging at 2 (short wavelength channel) and 4 (long wavelength channel) microns with a PSF FWHM of ∼2 pixels in both cases. The MIRI instrument in imaging mode, on the other hand, provides a FWHM of 0.22 arcsec (PSF FWHM of 2 pixels) for wavelengths ≥6.25 μm [2]. The NIRCam imaging of NGC 3132 used 8 dither points with an offset of approximately 6 arcsec, while MIRI imaging used a 1 × 2 tile mosaic with 8 dither points. The final NIRCam and MIRI images cover areas of approximately 150 × 150 arcsec^2 and 150 ×130 arcsec^2, respectively.

Images were downloaded from the MAST archive (calibration CRDS_VER11.16.3) and are neither continuum subtracted (free-free emission is included) nor background subtracted; the background regions of the MIRI images display significant flux that is thermal emission from the (cold) telescope and sunshade. In addition, although specific lines are targeted by specific narrow-band filters, additional (albeit weaker) lines may be present in some bandpasses (e.g., the F187N bandpass, which is dominated by Paα, is contaminated by He I lines). In order to determine the emission features present in each band, we have generated a simple model to predict the IR spectrum of the nebula, and compared it to previously published *Spitzer* observations, see Supplementary Figure 2, alongside the JWST bandpasses. Here we see, for example, that the MIRI F770W image is likely contaminated with H I and [Ar II] in certain regions. *Spitzer* spectroscopy indicates no sign of PAHs at 6.2, 7.7 and 8.6 μm and only a very weak 11.3 μm feature as well as cristalline silicates [3, 4]. This is usually associated to the presence of neutral PAHs [5]. As a result we have not included PAH emission contribution at 7.7 μm. On the other hand, *Spitzer* spectra do not cover the region below 5 μm so we have indicated that there could be a weak 3.3 μm feature.

In Supplementary Figure 3 we select three regions of the nebula observed through the NIRCam filter F212N, which we present, enlarged, in Supplementary Figure 4. The latter Figure presents image sequences consisting of archival HST images and the new JWST (ERO) images. These sequences illustrate the contrast between the smoothness of the emission from ionised gas vs. the clumpiness of H_2 emission, as well as the correspondence between dust extinction (most evident in the HST images) and the H_2 filaments and knots.

Supplementary Table 1 List of JWST filters used in this work and expected emission in the corresponding band.

Filter name	λ_1[1] (μm)	λ_2[1] (μm)	Emission features within bandpass	Date[2]	$T_{\rm exp}$[2] (sec)
			NIRCam		
F090W	0.795	1.005	[S III] 9069,9562 Å	2022-06-03	5841
F187N	1.863	1.884	H I Paα	2022-06-03	9277
F212N	2.109	2.134	H_2 (1,0) $S(1)$	2022-06-03	9277
F356W	3.140	3.980	H_2; Dust; PAHs?	2022-06-03	1460
F405N[3]	4.028	4.074	H I Brα		
F470N[3]	4.683	4.733	H_2 (0,0) $S(9)$		
F444W	3.880	4.986	H I Brα; H_2; Dust?	2022-06-03	2319×2
			MIRI		
F770W	6.6	8.8	H_2 (0,0) $S(5)$	2022-06-12	2708
F1130W	10.95	11.65	PAHs	2022-06-12	2708
F1280W	11.6	14.0	[Ne II] 12.8μm; H_2 (0,0) $S(2)$	2022-06-12	2708
F1800W	16.5	19.5	Warm dust; [S III] 18.6μm	2022-06-12	2708

[1] λ_1, λ_2: wavelengths at which the bandpass transmission is 50% of the peak transmission.

[2] Observing date and exposure time.

[3] Pupil wheel filter; used in combination with F444W.

Central star magnitudes

JWST has detected the central visual binary from F090W to F1800W (Supplementary Figure 5). At near-infrared wavelengths, the central star is faint and on the edge of the diffraction spikes from the nearby A-type star. From 7.7 μm longward, the central star is observed to increase in brightness, and at 18 μm it exceeds the flux from the A-type star.

We obtained optical magnitudes of the central star from the Hubble Source Catalogue version 3 [6]. The $F438W$, $F555W$ and $F814W$ Wide Field Camera 3 magnitudes in the AB system were converted to Jy. The calibrated 2D resampled NIRCam and MIRI observations available as i2d pipeline products were used to perform aperture photometry of the central star using the PHOTUTILS package [7]. A circular aperture was centered on the central star with radii corresponding to the 80% encircled energy radius tabulated in the relevant aperture correction tables, sufficient to include the majority of the central star flux. The tables JWST_nircam_apcorr_0004 and JWST_miri_apcorr_0008 were sourced from the JWST Calibration Reference Data System. Aperture photometry of the central source was performed with the error extension of the image included. Three circular sky apertures of the same radius were selected nearby the central star to best sample the challenging background. The background includes artefacts from the diffraction pattern of the A-type star nearby (more prominent in the NIRCam images) and the structured nebular background from NGC 3132. In the $F090W$, $F212N$, $F405N$ and $F470N$

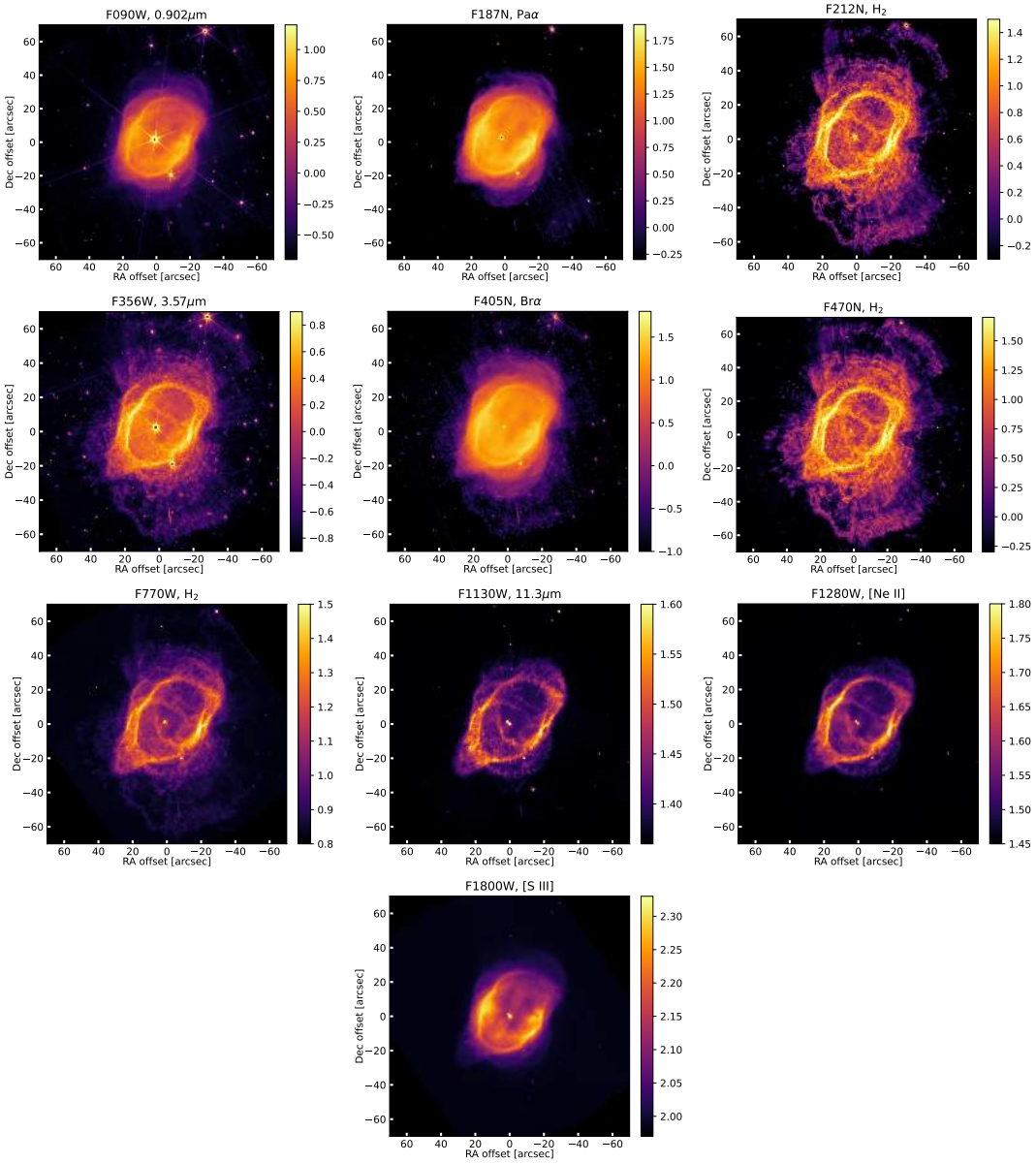

Supplementary Figure 1 JWST NIRCam and MIRI images of NGC 3132. North up and East is to the left. Colour bars indicate surface brightness in log(MJy ster^{-1}).

filters the dominant background and/or intrinsic faintness of the central star precluded any meaningful fluxes from being measured.

The sky background was estimated as the average of the median counts in each sky aperture, where the median was calculated using sigma clipping with $\sigma = 3$. The sky background was scaled to the aperture area A of the central star aperture before it was subtracted from the aperture sum. The flux of the central star was calculated as the sky subtracted aperture sum scaled by the MJy/sr to μJy conversion factor and the aperture correction sourced from the aperture correction tables. The uncertainty in the flux was estimated as $\sqrt{\sigma_p + 2\sigma_{\rm sky}}$ where σ_p is the PHOTUTILS aperture_sum_err and $\sigma_{\rm sky}$ is $A\sigma_b^2$, where σ_b is the average of the standard deviation of counts in each sky aperture.

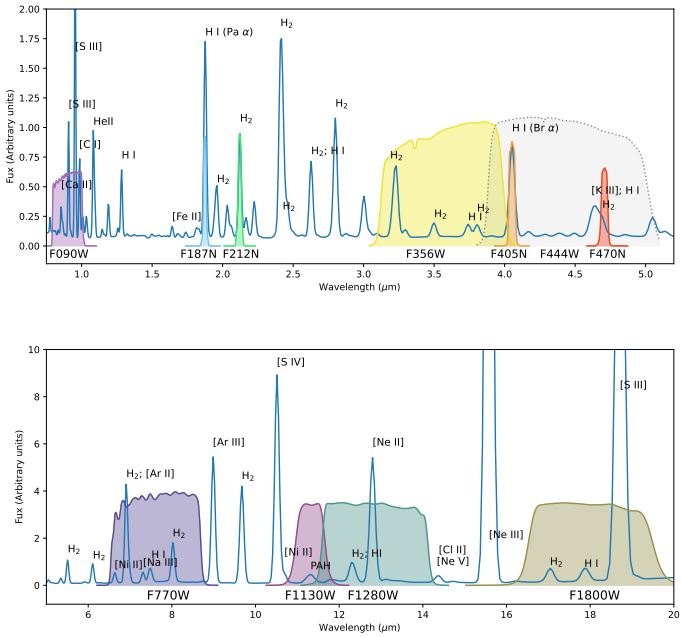

Supplementary Figure 2 Simulated IR spectrum of NGC 3132, overlaid with the JWST filters to demonstrate bandpass contamination. Top panel: the simulated spectrum of NGC 3132 between 0.8 and 5.2 μm (blue line) with, overlaid the JWST bandpasses (labelled coloured shapes). Bottom panel: the simulated spectrum of NGC 3132 between 5 and 20 μm (blue line) with, overlaid the JWST bandpasses (labelled coloured shapes).

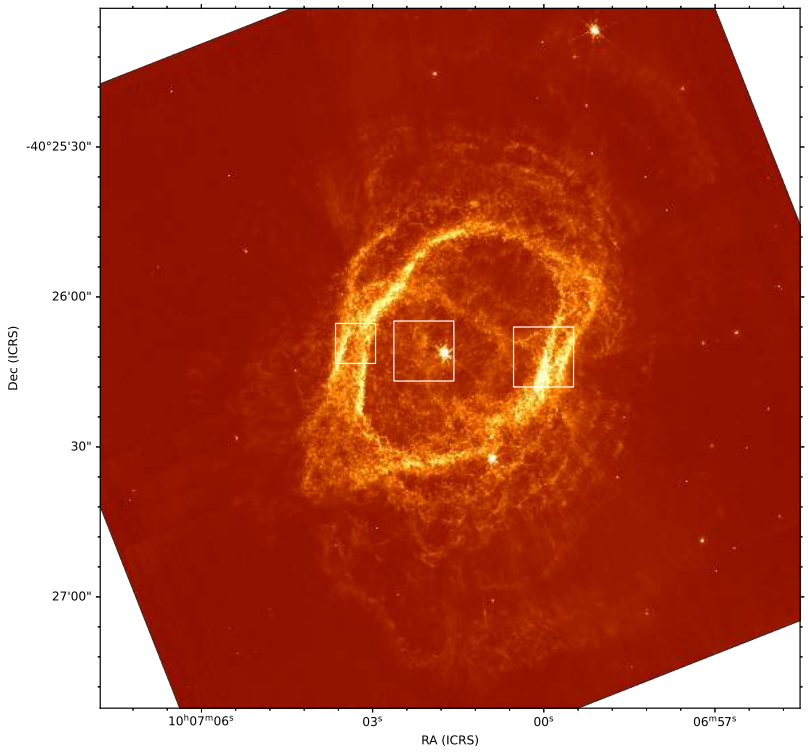

Supplementary Figure 3 JWST/NIRCam F212N image of NGC 3132. White squares indicate positions and sizes of "blowup" regions highlighted in Figure 4.

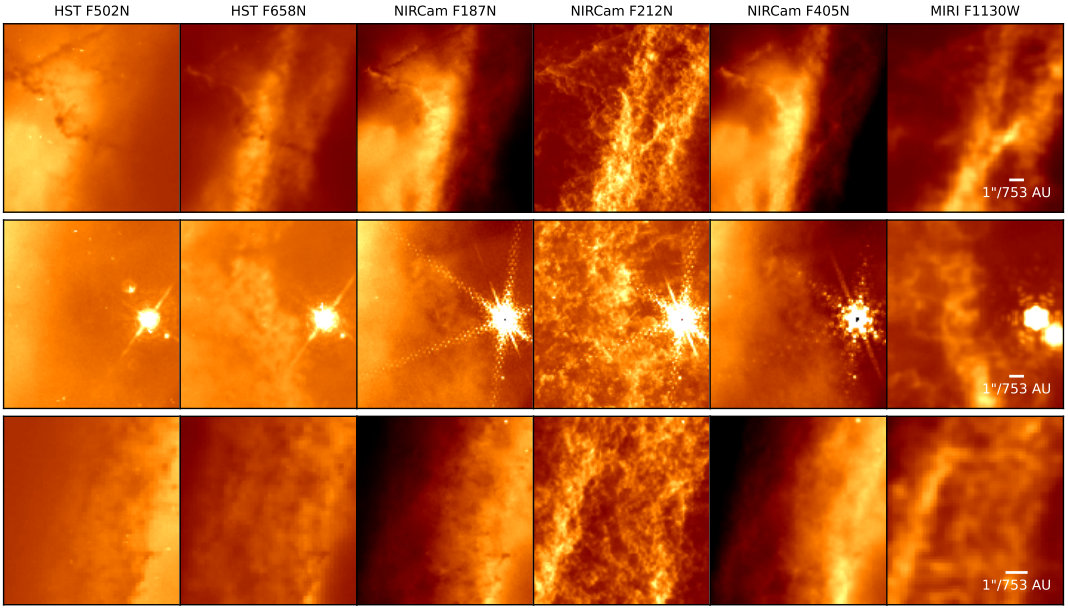

Supplementary Figure 4 The enlarged images of knots in three representative regions, indicated by white boxes in Figure 3: the West side of the ring (top row), near the centre of the ring (middle row) and the East side of the ring (bottom row). Filament structures stand out in the NIRCam F212N images. A few filaments are dusty, as clearly seen in the HST optical images (first two columns), but also in the NIRCam F187N and F405N images (third and fifth columns).

However, due to the complex sky background, these uncertainties are likely underestimates of the true uncertainty, which we estimate to be 5–10% of the flux.

Supplementary Table 2 gives the measured and dereddened fluxes using $A_V = 3.1E(B-V)$, where $E(B-V) = 0.09$ mag [8], and filter extinction ratios are from the Spanish Virtual Observatory Filter Profile Service [9, 10].

In Supplementary Figure 6 we present the PARSEC isochrones with the derived location of the A2V star.

Filter	F_ν (μJy)	Formal error*	$F_{\nu,0}$ (μJy)	Formal error*
WFPC3/F438W	1620.32	10.21	2274.64	14.3
WFPC3/F555W	1188.50	7.33	1556.61	9.6
WFPC3/F814W	560.27	3.29	654.18	3.8
NIRCam/F187N	130.43	4.65	135.77	4.84
NIRCam/F356W	50.78	5.31	51.67	5.41
MIRI/F770W	285.68	13.47	288.02	13.58
MIRI/F1130W	1445.32	2.46	1462.85	2.49
MIRI/F1280W	1362.75	5.85	1373.09	5.90
MIRI/F1800W	11344.60	20.93	11425.35	21.08

*The actual error on this photometric measurements is likely
* closer to 5-10% of the flux values.

Supplementary Table 2 Measured (F_ν) and dereddened ($F_{\nu,0}$) fluxes of the central star. To convert to magnitudes: $mag(AB) = -2.5 * log10(F_\nu$ [in Jansky]$) + 8.90$

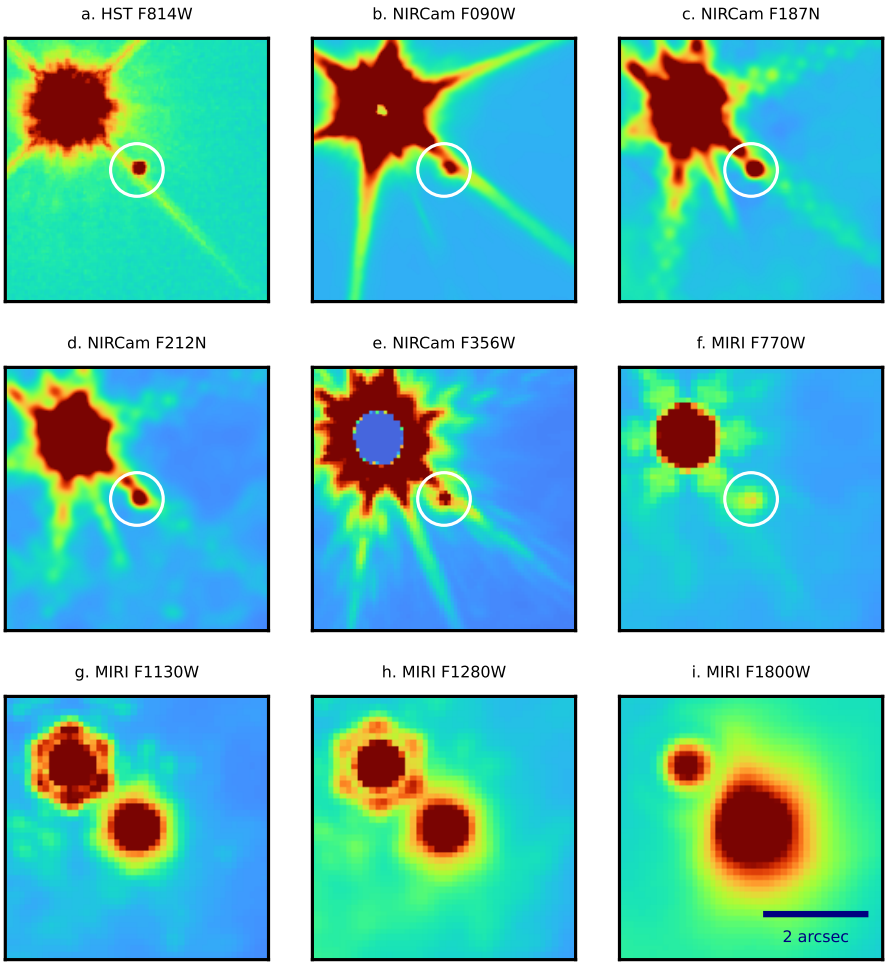

Supplementary Figure 5 Sections of the JWST images zooming in on the central stars. NIRCam F090W, F187N and F212N images are deconvolved with simulated PSFs. HST, NIRCam F356W and MIRI images are not deconvolved. Note that the slight offset of the positions of the central star in the F090W and F187N images is due to imperfect deconvolution due to the nearby saturated star.

Extended structure of the central star

Supplementary Figure 7 demonstrates the extended structure of the central star in the MIRI F1130W and F1800W band images. From the left to right column, we see the central, the A-type star, an example of a saturated star, and the simulated PSF. The images are oriented such that North is 145 degrees clockwise. An example image of a saturated star is from the Tarantula Nebula region, which was observed as a part of the first image program (PID 2729). The coordinate of this saturated star is RA=05h38m33.61s and Dec=−69d04m50.5s. The MIRI PSF is simulated based on Webb PSF software version 1.1.0 (https://jwst-docs.stsci.edu/jwst-mid-infrared-instrument/miri-performance/miri-point-spread-functions). The top row shows the images, and the second and third rows show radial profiles, which are sliced in horizontal and vertical directions across the peak (blue lines). Dotted lines indicate the

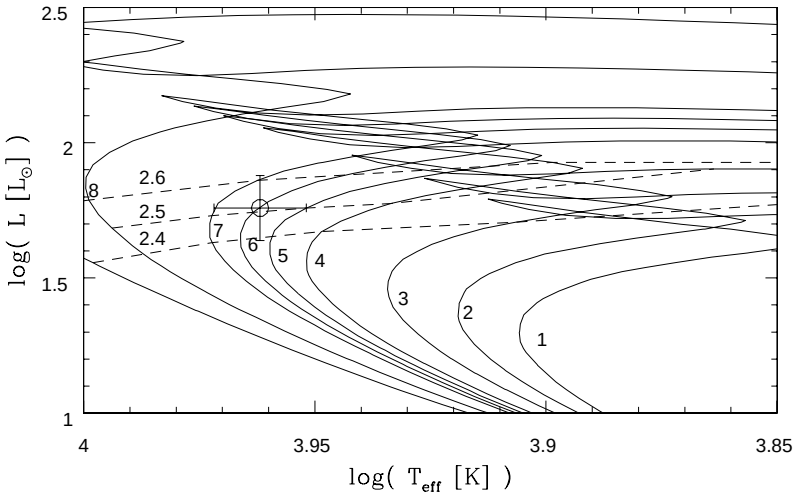

Supplementary Figure 6 PARSEC [11] isochrones with the location of the A2 V star. The isochrones are labelled in order of descending age : 9, 8, 7, 6, 5.6, 5.3, 5, 4 in units of 10^8 yr. The dashed lines connect points of constant mass, labelled in solar units. The error bar on the horizzontal axis is the temperature uncertainty given by *Gaia*, ±200 K. The error bar on the vertical axis is based on a conservative 0.25 mag error on the absolute magnitude.

data points that are strongly affected by other factors, such as bright neighbouring stars or detector saturation. The central star is mildly saturated in the F1800W image, with data quality flags of about 5—8 pixels across the peak, so that the data within the 10 pixels from the peak of the central star are plotted as dotted lines. On the central star radial profiles of F1800W, green lines demonstrate the simulated radial profile with 0.44 arcsec radius flat-intensity 'disk'. This shows that the central star is extended at a scale of $\gtrsim$0.8 arcsec. In the radial profiles, the PSF is also plotted as an orange line, which has a FWHM of 0.58 arcsec at F1800W.

Supplementary Figure 7 demonstrates that the central star is clearly extended more than the PSF. On the central star radial profiles, green lines demonstrate the radial profile with a 0.44 arcsec radius, flat-intensity 'disk'. In reality, the intensity gradually decreases radially, rather than a flat intensity with a cliff edge, and the tailing of this gradual decrease continues beyond 0.4 arcsec.

Morpho-kinematic modelling

In Figure 3 we have presented the 3D morpho-kinematic reconstruction of the ionised region of NGC 3132 using the interactive morpho-kinematic modelling software *Shape* [12]. In addition to the new images from JWST, spectroscopic reference data for the reconstruction are position-velocity diagrams from the San Pedro Mártir Kinematic Catalogue of Galactic Planetary Nebulae ([13, 14]).

An assumption is made on the current velocity field in order to map the Doppler-shift to a 3D position of that image element. We assume an overall homologous velocity field [15], except locally for some protrusions (see below).

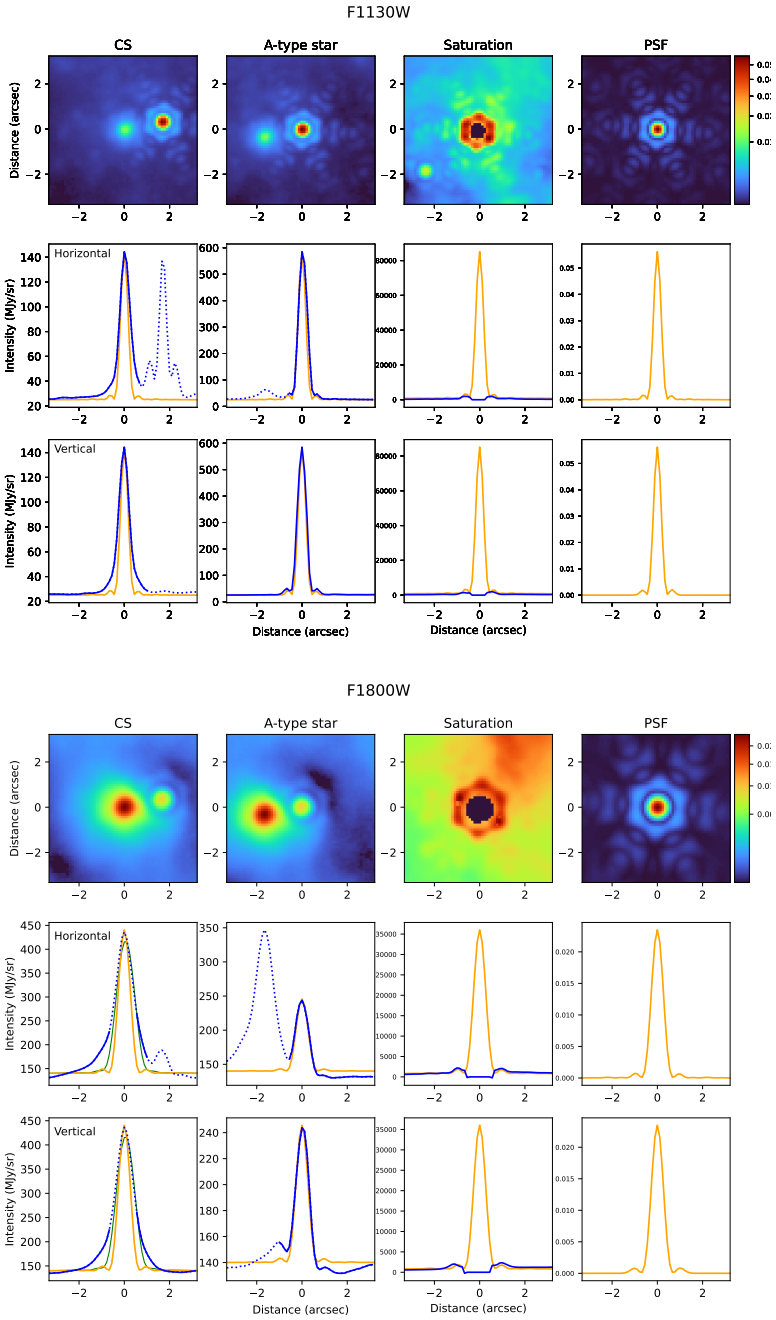

Supplementary Figure 7 Demonstration of the extended structure of the central star in the MIRI F1130W (top panel) and F1800W (bottom panel) band images. From the left to right column, the central star, the A-type star, an example of a saturated star, and the simulated PSF. The top row displays the images, and the second and third row show radial profiles, which are sliced in the horizontal and vertical directions across the peak (blue lines). Dotted lines indicate the data points strongly affected by other factors, such as bright neighbouring stars or detector saturation for the F1800W image. In the radial profiles, the PSF is also plotted as an orange line.The central star is clearly extended more than the PSF. On the central star radial profiles of the F1800W image, the green line demonstrates the radial profile of a 0.44 arcsec-radius, flat-intensity 'disk'.

The velocity field is 1 km s^{-1} arcsec^{-1}. This value ensures that the cross-section of the main shell is approximately circular. We estimate the uncertainty to be of the order of 30%. Note that the stretching of the structures along the line of sight is proportional to this value. In other words, the shape of the nebula along the line of sight is linearly related to the component of the velocity vector. This model of the inner ionised cavity supersedes or rather, completes, the barrel or "diabolo" model [16] in view of more sensitive spectroscopy that allowed us to detect the faint, and fast, closed ends of the ellipsoid along its major axis, which is close to the line of sight.

In Supplementary Figure 8 we show the slit positions and resulting position-velocity diagram (top row: observed, bottom row: simulated) reconstruction with *Shape*. A 3D fly through the 3D volume can be found at this link. The position-velocity diagrams in Supplementary Figure 8 are effectively 2D renditions of the spectral line shape as we move along the slit. The slit positions are indicated.

In the final step of our morpho-kinematic model (Figure 3), we place two complete shells of non-uniform, filamentary material around the central star to match the observed size of the H_2 halo. The inner shell ranges from 33 to 45 arcsec from the central star, and the second ranges from 60 to 70 arcsec. These are illuminated through a partially opaque ellipsoid (approximately corresponding with the ellipsoid containing the ionised nebula) that has reduced opacity around the poles and has an overall porous opacity.

At this point we are only interested in testing the possibility that the opacity of the walls of the central cavity within which the exciting central star resides, could be the cause of the overall emissivity distribution and features. The central star is made to radiate as a blackbody. We have then used a simple proxy for the various radiative processes that are at work here, i.e., isotropic scattering on dust. Since we expect dust to dominate the transport of the exciting radiation, this is a reasonable first test, with the details being irrelevant for this simple geometric simulation. A spherical density modulation was also imposed with *ad hoc* spacing responding to the following modulation: $\rho/\rho_0 = 0.3 + \sin(0.8\ r/\mathrm{arcsec})^{10}\ \sin(1.4\ r/\mathrm{arcsec})^2$. This generates the arch pattern.

This type of painstaking morpho-kinematic modelling is critically dependent on images at different wavelengths as well as spatially-resolved spectroscopy. On the basis of this type of data driven 3D model, we can now understand structures first revealed by JWST such as the H_2 halo and the dusty central stars.

References

[1] Pontoppidan, K., Blome, C., Braun, H., Brown, M., Carruthers, M., Coe, D., DePasquale, J., Espinoza, N., Garcia Marin, M., Gordon, K.D., Henry, A., Hustak, L., James, A., Koekemoer, A.M., LaMassa, S., Law, D., Lockwood, A., Moro-Martin, A., Mullally, S.E., Pagan, A., Player, D.,

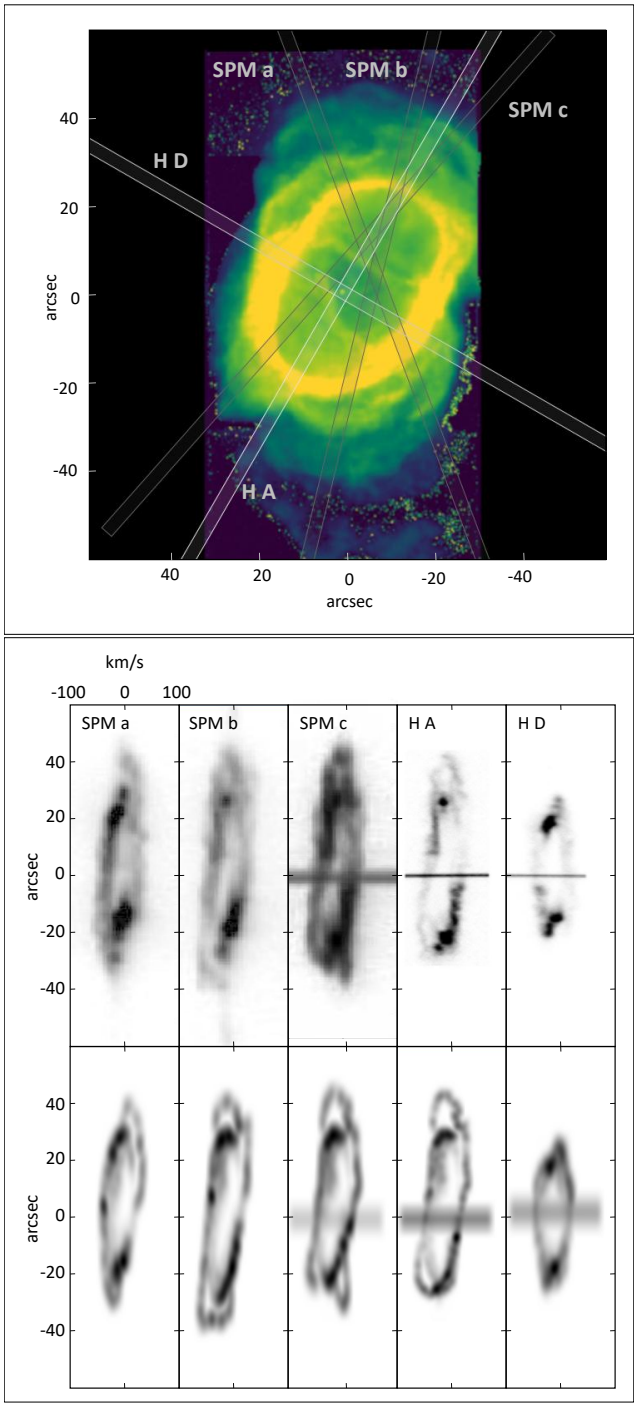

Supplementary Figure 8 Position velocity data and model to achieve the morpho-kinematic model of PN NGC 3132. Top figure: a MUSE [N II] image of NGC 3132 with the slit positions marked. The three slits from [13] are marked in grey and the two slits from [14] are in white. Bottom figure, top row: observed position-velocity diagrams for the [N II] nebular line along the different slits. Bottom figure, bottom row: corresponding modelled position-velocity diagrams using *Shape*. The heavy horizontal lines in the last three columns are the continuum emission from the A2 V star.

Proffitt, C., Pulliam, C., Ramsay, L., Ravindranath, S., Reid, N., Robberto, M., Sabbi, E., Ubeda, L.: The JWST Early Release Observations. arXiv e-prints, 2207–13067 (2022)

[2] Bouchet, P., García-Marín, M., Lagage, P.-O., Amiaux, J., Auguéres, J.-L., Bauwens, E., Blommaert, J.A.D.L., Chen, C.H., Detre, Ö.H., Dicken, D., Dubreuil, D., Galdemard, P., Gastaud, R., Glasse, A., Gordon, K.D., Gougnaud, F., Guillard, P., Justtanont, K., Krause, O., Leboeuf, D., Longval, Y., Martin, L., Mazy, E., Moreau, V., Olofsson, G., Ray, T.P., Rees, J.-M., Renotte, E., Ressler, M.E., Ronayette, S., Salasca, S., Scheithauer, S., Sykes, J., Thelen, M.P., Wells, M., Wright, D., Wright, G.S.: The Mid-Infrared Instrument for the James Webb Space Telescope, III: MIRIM, The MIRI Imager. Publ. Astron. Soc. Pac. **127**(953), 612 (2015)

[3] Delgado-Inglada, G., Rodríguez, M.: C/O Abundance Ratios, Iron Depletions, and Infrared Dust Features in Galactic Planetary Nebulae. Astrophys. J. **784**, 173 (2014)

[4] Mata, H., Ramos-Larios, G., Guerrero, M.A., Nigoche-Netro, A., Toalá, J.A., Fang, X., Rubio, G., Kemp, S.N., Navarro, S.G., Corral, L.J.: Spitzer mid-infrared spectroscopic observations of planetary nebulae. Mon. Not. R. Astron. Soc. **459**(1), 841–853 (2016)

[5] Cox, N.L.J., Pilleri, P., Berné, O., Cernicharo, J., Joblin, C.: Polycyclic aromatic hydrocarbons and molecular hydrogen in oxygen-rich planetary nebulae: the case of NGC 6720. Mon. Not. R. Astron. Soc. **456**(1), 89–93 (2016)

[6] Whitmore, B.C., Allam, S.S., Budavári, T., Casertano, S., Downes, R.A., Donaldson, T., Fall, S.M., Lubow, S.H., Quick, L., Strolger, L.-G., Wallace, G., White, R.L.: Version 1 of the Hubble Source Catalog. Astron. J. **151**(6), 134 (2016)

[7] Bradley, L., Sipőcz, B., Robitaille, T., Tollerud, E., Vinícius, Z., Deil, C., Barbary, K., Wilson, T.J., Busko, I., Donath, A., Günther, H.M., Cara, M., Lim, P.L., Meßlinger, S., Conseil, S., Bostroem, A., Droettboom, M., Bray, E.M., Andersen Bratholm, L., Barentsen, G., Craig, M., Rathi, S., Pascual, S., Perren, G., Georgiev, I.Y., De Val-Borro, M., Kerzendorf, W., Bach, Y.P., Quint, B., Souchereau, H.: astropy/photutils:. Zenodo (2022).

[8] Monreal-Ibero, A., Walsh, J.R.: The MUSE view of the planetary nebula NGC 3132. Astron. Astrophys. **634**, 47 (2020)

[9] Rodrigo, C., Solano, E., Bayo, A.: SVO Filter Profile Service Version 1.0. IVOA Working Draft 15 October 2012 (2012).

[10] Rodrigo, C., Solano, E.: The SVO Filter Profile Service. In: XIV.0 Scientific Meeting (virtual) of the Spanish Astronomical Society, p. 182 (2020)

[11] Marigo, P., Girardi, L., Bressan, A., Rosenfield, P., Aringer, B., Chen, Y., Dussin, M., Nanni, A., Pastorelli, G., Rodrigues, T.S., Trabucchi, M., Bladh, S., Dalcanton, J., Groenewegen, M.A.T., Montalbán, J., Wood, P.R.: A New Generation of PARSEC-COLIBRI Stellar Isochrones Including the TP-AGB Phase. Astrophys. J. **835**(1), 77 (2017)

[12] Steffen, W., Koning, N., Wenger, S., Morisset, C., Magnor, M.: Shape: A 3d modeling tool for astrophysics. IEEE Transactions on Visualization and Computer Graphics **17**(4), 454–465 (2011).

[13] López, J., Richer, M., García-Díaz, M.T., Clark, D., Meaburn, J., Riesgo, H., Steffen, W., Lloyd, M.: The san pedro mártir kinematic catalogue of galactic planetary nebulae. Revista mexicana de astronomía y astrofísica **48**(1), 03–07 (2012)

[14] Hajian, A.R., Movit, S.M., Trofimov, D., Balick, B., Terzian, Y., Knuth, K.H., Granquist-Fraser, D., Huyser, K.A., Jalobeanu, A., McIntosh, D.: An Atlas of [N II] and [O III] Images and Spectra of Planetary Nebulae. Astrophys. J. Suppl. Ser. **169**(2), 289–327 (2007).

[15] Zijlstra, A.A.: The infrared [WC] stars. Astrophysics & Space Science **275**, 79–90 (2001)

[16] Monteiro, H., Morisset, C., Gruenwald, R., Viegas, S.M.: Morphology and Kinematics of Planetary Nebulae. II. A Diabolo Model for NGC 3132. Astrophys. J. **537**(2), 853–860 (2000)